The Design and Fabrication of a 3D Printed Origami Wheel

Undergraduate Honors Thesis

Presented in Partial Fulfillment of the Requirements for
Graduation with Distinction in the
Department of Mechanical Engineering at
The Ohio State University

By

Benjamin Patrick Rhoads,

Undergraduate Program in Mechanical Engineering

The Ohio State University

2015

Thesis Committee:

Dr. Hai-Jun Su, Advisor

Dr. Carlos Castro

Abstract

Automobiles are complex machines, in part due to the transmission, suspension, and steering mechanism. By replacing the traditionally static tire with a deformable wheel that dynamically changes radius, the mechanical complexity of these three sub-assemblies can be reduced. Reducing the mechanical complexity lowers the cost and required maintenance of a vehicle, all of which are desirable traits for extraterrestrial rovers. A small proof-of-concept robot was built to demonstrate the feasibility of deformable wheels.

A deformable wheel was developed based on the origami spring fold pattern pioneered by Jeff Benyon. Benyon's fold pattern consists of several sections that compress when under load and spring back to their original form when the load is removed. To be suitable as a deformable wheel, the origami spring fold pattern was modified to increase contact area with the ground and adjusted to accommodate an axle. The overall theoretical change in radius of the wheel using the modified fold pattern was found to be approximately 50%. This new origami pattern was used to create the deformable wheels for the proof-of-concept robot.

While origami is traditionally performed with paper, paper was not used to create the deformable wheel because it lacks load bearing capacity and has a low fatigue life. Shape Deposition Manufacturing (SDM) and a novel 3D printed manufacturing method were tested to create a laminate suitable for proof-of-concept origami

mechanisms. The 3D printed method provided the best results and was scalable to large origami patterns, while the SDM process was not. The 3D printed laminate has an estimated fatigue life of 10^6 cycles and in testing carried ten times the load of cardstock paper.

The proof-of-concept robot successfully changed speed, drove over obstacles, and was able to steer without a dedicated transmission, steering mechanism, or suspension.

Dedicated to my loving family and supportive friends

Acknowledgments

I would like to begin by thanking Dr. Hai-Jun Su, my adviser, for allowing me to perform this research. Additionally, I would like to thank Dr. Su for providing lab space as well as the necessary equipment to complete this project.

The financial support I have received from the Ohio State University College of Engineering and the Ohio State University Undergraduate Student Government made this project possible. I am very appreciative of their support.

The members of the Design, Innovation, and Simulation Laboratory who I have worked with on this project were instrumental in its success; especially Venkat Venkiteswaran and Yu She who taught me to use the equipment in the DISL. I am very grateful for their patience and guidance.

I would also like to thank Michael Vernier for his never ending assistance. Whenever I encountered a roadblock, Mike always provided words of wisdom and pertinent suggestions. I would not have been able to accomplish as much as I have without him. I especially thank him for teaching me everything I know about PCB manufacturing and for always reminding me that 'ninja soldering' can fix every problem.

Additionally, Amy Koehler graciously proofread this thesis multiple times and provided insights into composite analysis, and for that I thank her.

Finally, my parents, Greg and Susan, provided infinite amounts of support and encouragement throughout this project and were crucial to its success.

Table of Contents

Page

List of Tables

List of Figures

Chapter 1: Introduction

This chapter outlines the motivation for this research, provides an overview of existing literature in the field, and describes the goals of this thesis in detail.

1.1 Motivation

Modern automobiles are complex integrated systems with thousands of moving components. The suspension, transmission, and steering mechanisms are three vehicular subsystems that drive mechanical complexity. These subassemblies are complex, in part, because of the assumption that the car tire maintains a constant radius while driving. If a chassis has four wheels that can change radius independently, the functions of suspension, transmission, and steering can be encapsulated in the deformable wheels. The mechanical complexity of the chassis then depends only on the actuation required to deform the wheels. Reducing the mechanical complexity of the vehicle reduces costs, assembly time, and the amount of maintenance required. An extraterrestrial rover, for example, greatly benefits from reduced maintenance since it is difficult to maintain a vehicle on the moon.

One way of achieving a dynamically deformable wheel is by using origami, the Japanese art of paper folding. Complex 3D mechanisms can be folded from a 2D sheet using the principles of origami. Paper is traditionally the material of choice

for origami; however, it has poor engineering properties, namely low load carrying capacity and a low fatigue limit. Shape Memory Alloy (SMA) actuators are typically used with origami mechanisms because they are lightweight. The response time of a SMA is on the order of a few seconds, which is not fast enough for a deformable wheel [20]. Thus, it is desired to create a material capable of supporting the weight of traditional actuators, such as servo motors, which do have fast enough response times for a deformable wheel. Some manufacturing methods exist to create foldable materials that exhibit better engineering properties than paper. But, many existing manufacturing techniques at the 'desktop' scale do not simultaneously provide high fatigue life, material strength, and the ability to produce arbitrary origami designs.

The goal of this thesis is threefold: to describe a novel manufacturing method for creating origami laminates, to demonstrate an origami pattern that can be used as a deformable wheel, and to demonstrate that the functions of suspension, transmission, and steering can be encapsulated with deformable wheels by building a proof-of-concept robot.

1.2 Literature Review

1.2.1 Existing Origami Manufacturing Methods

Origami is the traditional Japanese art of paper folding and can be abstracted as a series of panels connected by folds. Origami principles have been adapted to a wide array of manufacturing techniques, ranging from nanoscale DNA stapling to fabricating metal hinges for satellite solar arrays [3, 12]. At the 'desktop' (1cm to 30cm) scale, several materials and methods are used to create origami mechanisms. Typically, origami prototypes are made from paper or polyester [24]. If strength is

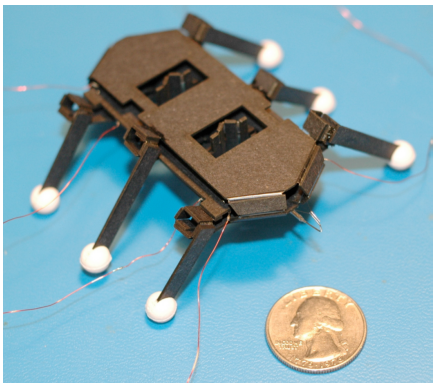

Figure 1.1: Small Robot Created from Posterboard Based SCM [10]

required, the prototype is usually made from a material with rigid sections attached to a flexure [10]. Gaps in the rigid sections allow the flexure to bend and crease.

Paper and polyester are both easy to obtain and fold, and are often used to prototype origami fold patterns. Fold lines can be printed on paper or quickly perforated in polyester with a laser cutter. However, mechanisms created from paper are primarily actuated by Shape Memory Alloys (SMAs) because the structures cannot support the weight of more traditional actuators such as electric motors. Paper also has low shear strength and can tear easily. Polyester does not tear as easily and has a fatigue life of 10^6 cycles [8]. However, polyester can also only carry limited loads.

To overcome the load carrying and fatigue limitations of paper and polyester, Smart Composite Manufacturing (SCM) techniques were adapted to the desktop scale [10, 29]. SCM is the process of creating foldable laminates from laser micromachined layers of carbon fiber, polyimide, and other polymers. SCM is used to create microrobots at the 1 cm and smaller scale [4]. The desktop scale SCM adapation developed

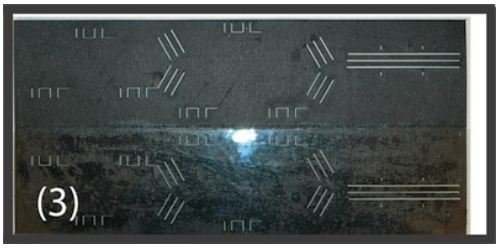

Figure 1.2: Posterboard workpiece with fold areas laser cut and polyester film attached to bottom panel [13]

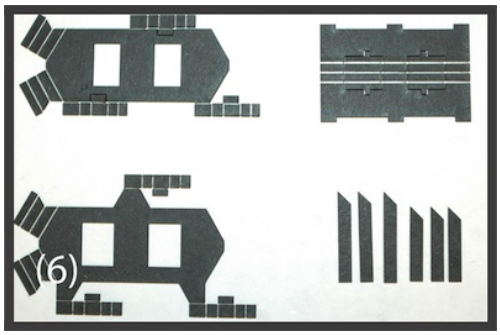

Figure 1.3: Mechanims after being released from the workpiece [13]

by Hoover uses a polyester flexure sandwiched between two layers of rigid posterboard or S-2 glass fiber composite [10].

The desktop variant of SCM begins by laser cutting rigid poster board or S-2 fiber glass. Two copies of the desired object are made, one to be placed on top of the flexure, and one to be placed on the bottom. Areas where a fold is desired are removed from both the top and bottom copy of the rigid material, as seen in Figure 1.2. A layer of polyester is then glued to one of the copies, and the other copy is folded over. The sandwich is then ran through a hot roll laminator to set the adhesive between the polyester flexure and rigid material. After the adhesive has cured, the workpiece is placed back in the laser cutter and the outlines of the desired parts are cut, with the end result shown in Figure 1.3. The polyester flexure provides high fatigue life while the rigid material panels provide load carrying capacity. For some origami patterns, desktop SCM provides a quick way to prototype robots. However, this manufacturing method cannot be used for all origami patterns without significant human intervention.

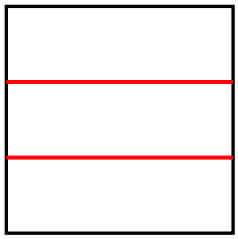

Figure 1.4: Ideal Desktop SCM Folds

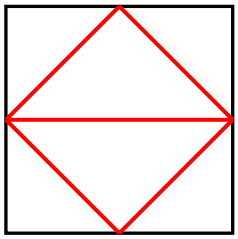

Figure 1.5: Non Ideal Folds

Desktop scale SCM works well when regions of material are not separated from exterior edges by folds, as shown in Figure 1.4. The rectangle formed between the two red fold lines is connected to the exterior edge of the material on both sides. Figure 1.5 demonstrates non-ideal folds; the red fold lines intersect and form isolated sections of rigid material. The two triangles created from the intersections of the fold lines are isolated from exterior edges. When the rigid material is folded over onto the polyester flexure, the isolated sections will fall off and need to be placed by hand. For a design with only a few isolated sections, this may be acceptable. However, if the pattern in Figure 1.5 is tessellated to 100 units, the manufacturing time increases significantly. Additionally, if the rigid materials sandwiching the polyester flexure are not aligned properly when placed by hand, the joint will fold at an incorrect angle.

Another manufacturing method uses thin pieces of PVC sewn between two pieces of cloth [14]. The cloth provides a region that is foldable and the PVC pieces provides rigidity. This method is time intensive, each piece of PVC needs placed by hand before the cloth is sewn. However, this manufacturing method allows edges of origami fold patterns to be mechanically joined. Some designs require glue joints, which create a weak area in the structure. This is especially a problem for origami mechanisms which

Figure 1.6: Wheel with Extractable Spokes for Additional Traction

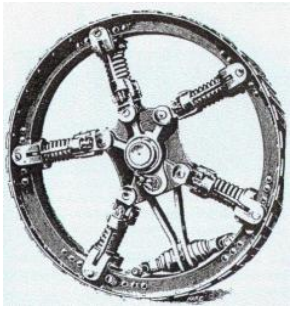

Figure 1.7: Wheel for All Terrain Vehicle with Internal Springs

are constantly actuated along the joint. When the material is cloth, the edges can be sewn together, providing a mechanical connection. In a dynamic origami mechanism, the mechanical connection is more robust than a glued joint.

To the author's knowledge, a method to create a laminate that is plastically deformable, has rigid in-plane sections, and is scalable to an arbitrary origami design does not exist in the literature.

1.2.2 Existing Deformable Wheel Designs

In the early 1900s, farm equipment manufacturers developed two types of deformable wheels, shown in Figure 1.7 and Figure 1.6 [25]. The wheel in Figure 1.7 was developed by Tolotti & Pavesi, an Italian tractor company, and has spikes mounted underneath the rim which rotate outward to provide more traction. The wheel in Figure 1.6, developed by Fowler, has internal springs that functioned as a rudimentary suspension and allowed the wheel rim to deform slightly as obstacles were encountered. The ideas of gaining additional traction through expanding spikes and using a

Figure 1.8: Michelin Tweel^{TM} [18]

deformable wheel as a portion of the suspension drove many future deformable wheel designs.

Michelin has adapted the principles behind the Fowler design in their Tweel^{TM}, shown in in Figure 1.8. The Tweel^{TM} consists of a semi-rigid outer rim and flexible spokes capable of deflecting. The deflection of the Tweel^{TM} spokes increases torque as load is added to the vehicle; as more weight is carried, the radius passively decreases. The deflection of the spokes also smooth out small irregularities in the terrain [18].

Wheels that change radius have also been used in consumer toys. Lewis Galoob Toys developed a remote control (RC) truck, "The Animal", which featured 'claws' that would extend past the wheel diameter to help overcome obstacles. When the torque on the tires exceeded a certain amount, the claws extend due to a cam mechanism [16]. While the 'claws' adapt to the torque requirements of the RC truck, they are not user-controlled and are either extended or hidden inside the wheel.

The Fowler tire, Michelin Tweel, and Lewis Galoob wheel are all passive; the user cannot explicitly control the state of the wheel. On the other hand, the Tolotti wheels are user-controllable but binary; the wheel is either expanded or it is not. A fully user-controllable deformable wheel was developed at the University of Delaware

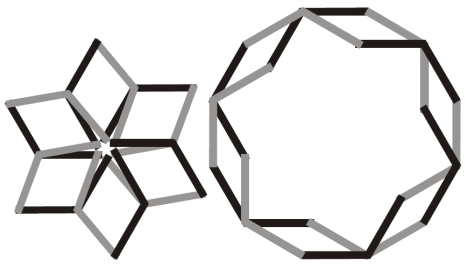

Figure 1.9: Deformable Wheel Using Hoberman Mechanisms [2]

using single degree of freedom expanding polyhedral structures [1]. The expanding wheel was based on Hoberman prismatic joints, and is shown in Figure 1.9. A wheel constructed of Hoberman joints requires several revolute and prismatic joints. As the wheel becomes smaller, it becomes more difficult to machine these joints. Additionally, it is nontrivial to actuate a Hoberman based wheel while also mounting it to a driven axle; the entire structure is continuously moving as the wheel is expanded and contracted.

A simpler, fully controllable wheel was created using the common origami 'magic ball' pattern, shown in Figure 1.11[15]. The wheel is made by tessellating the common origami 'waterbomb' fold pattern, shown in Figure 1.10. The 'magic ball' origami wheel can change radius dynamically and is simple to actuate: squeezing the wheel directly increases the radius. However, the 'magic ball' pattern requires that two edges be glued or attached together, which introduces a weak spot in the wheel. The sewn cloth manufacturing method described in Section 1.2.1 eliminates the week spot but the manufacturing process is time consuming.

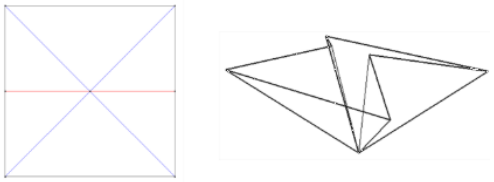

Figure 1.10: Single 'Water Bomb' Unit [15]

Figure 1.11: 'Magic Ball' Origami Wheel Design [15]

A design flaw with the Hoberman and origami 'magic ball' deformable wheels is that the weight of the robot must be lifted by the actuation mechanism. In order for the wheel to change shape, the entire mass of the robot must be lifted. To overcome this, a 'passive leg' deformable wheel was developed [31]. The passive leg allows the wheel to deform without lifting the weight of the robot. Similar to the "The Animal" wheel, the main limitation of the passive leg design is that the radius change is binary, there are not any states between the larger and smaller radii.

1.3 Organization of this Thesis

The rest of this thesis is organized as follows.

Chapter 2 describes the design and analysis of a deformable wheel using origami techniques.

Chapter 3 presents two manufacturing techniques for creating foldable laminates suited for prototyping origami mechanisms.

Chapter 4 describes the design of a small proof-of-concept robot to demonstrate the feasibility of deformable wheels.

Finally, Chapter 5 summarizes the results of the thesis, and gives suggestions to further this work.

Chapter 2: Design of a Foldable Wheel

2.1 Modified Benyon Spring Wheel Design

An origami 'spring', shown in Figure 2.1, was developed by Jeff Benyon which compresses under load and springs back when the load is removed. As the spring is compressed, the individual sections of the spring expand radially. Each individual section can be thought of as a spiral discretized by n segments. When the spring is compressed the segments unspiral outward, and when the spring is expanded the segments spiral inward. The radial deformation of the sections suggested the origami spring could be the basis for a deformable wheel. A single section of the spring was isolated and modified to produce a deformable wheel.

Figure 2.1: Jeff Benyon's Origami Spring With Five Sections

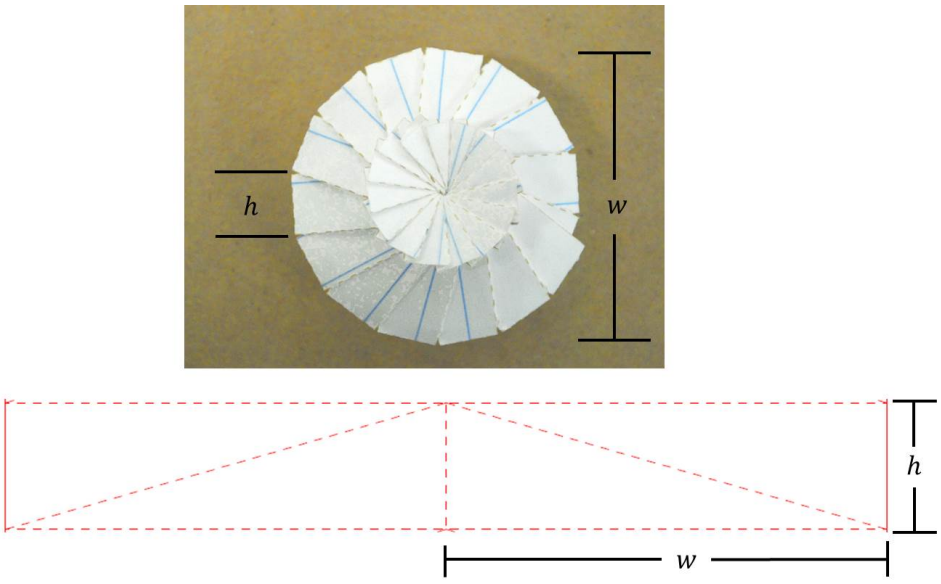

Figure 2.2: Single Segment of Jeff Benyon's Fold Pattern and Completely Folded Wheel

A single element of the Benyon origami spring fold pattern can be seen in Figure 2.2. There are two design parameters for the fold pattern, w, the width of a segment, and h, the height of a segment. The diameter of the folded wheel is w while h determines the edge length of the wheel, as shown in Figure 2.2. The single element of Figure 2.2 is tessellated vertically n times to achieve the Benyon origami fold pattern, which can be seen in Figure A.1 of Appendix A. The number of segments, n, required to form a complete wheel is explored further in Section 2.2.

While providing radial deformation, the Benyon spring pattern was not immediately suitable for a deformable wheel. The original fold pattern did not have any accommodation for an axle; all of the segments met at a single point in the center of the spring. To accommodate an axle, a new design parameter, δ, was introduced and is shown in Figure 2.3. The endpoints of the horizontal lines in the original pattern

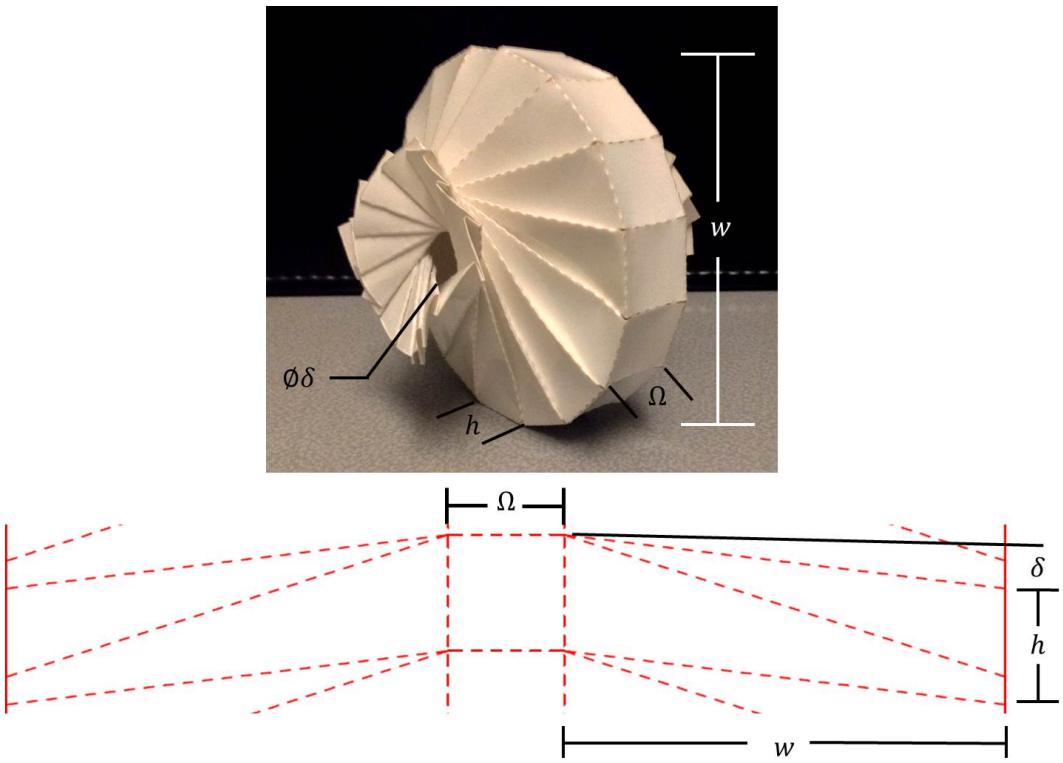

Figure 2.3: Modified Fold Pattern With Axle Hole and Wheel Width

were shifted down by δ, which caused an axle hole to form in the middle of the wheel with diameter δ. After the testing performed in Chapter 3, it was determined that the contact edge of the wheel with the ground was typically a failure point. To help distribute the load at the contact point, an additional design parameter, Ω, was introduced to add 'width' to the wheel. The value of Ω did not affect the deformability of the wheel and can be chosen arbitrarily. For aesthetic purposes, Ω was always chosen to match h. Determining how δ and Ω affected the fold pattern was performed both experimentally through trial and error folding and with the help of a wheel model built in Mathematica.

The Benyon spring inspired deformable wheel has four main limitations. The wheel does not have a perfectly circular contact surface, instead there are n line segments forming the circumference. If n is large, the wheel has an approximately circular contact surface, but, if n is small, the rotation is not smooth and induces chassis vibration. Another limitation of the design is that significant axial deformation is required to accomplish meaningful radial deformation, which is explained further in Section 2.2. Additionally, the wheel can require significant force to actuate; each fold stores spring energy which must be overcome to deflect the wheel. The final limitation of the origami spring wheel is that there is a finite amount of deformation that can be achieved; the wheel cannot go from a diameter w to having a diameter of 0. The minimum achievable radius and optimization techniques for the design are discussed in Section 2.3.

2.2 Geometric Model

The origami wheel was approximated as an n-sided regular polygon (hexagon, octagon, dodecagon, etc), shown in Figure 2.4. When the wheel in Figure 2.4 was fully compressed, it was approximated as a 14-sided polygon, and when fully expanded it was approximated as an 11-sided polygon. As the wheel expanded or contracted, the spiraling motion of the segments caused the number of exterior sides to change. As the wheel was compressed the segments unspiralled, causing n to increase, which caused the overall diameter of the wheel to increase. Throughout the deformation, the edge length of the polygon, h, remained constant, which allowed the n-sided polygon approximation to be made.

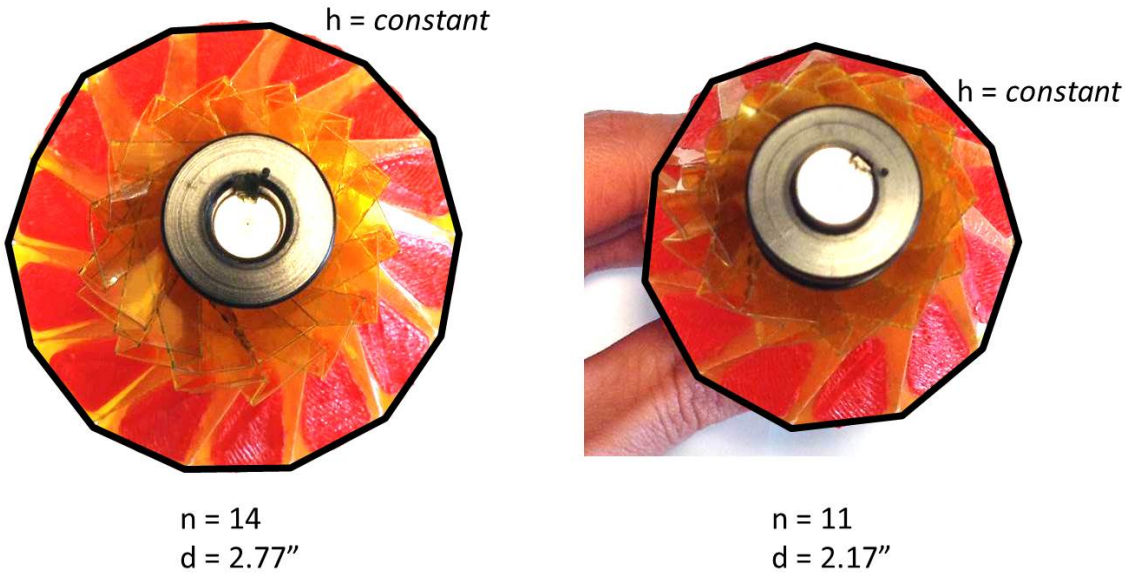

Figure 2.4: n-sided Polygon Approximation

Using the n-sided regular polygon approximation, a governing equation relating the three relevant design parameters h, w, and δ, and the axial deformation of the wheel x, with the number of sides of the approximating polygon, n was found and is shown in Equation 2.1. A full derivation of the equation is given in Appendix B. The design parameter Ω is not present in the n-sided polygon model; Ω does not affect the geometry of the mechanism. Originally it was thought that the domain limiting features of Equation 2.1 explained why the wheel had a maximum amount of deformation. However, setting $\delta = 0$ and examining the domain of the equation revealed that the limiting factors corresponded to trivial physical solutions which are found and explained in Appendix B.

$$n = \frac{\pi}{\sin^{-1}\left(\frac{h}{\sqrt{-\frac{h^2w^2\left(\delta h + w^2\right)}{\left(\delta(\delta+h)+w^2\right)^2} + h^2 + \frac{hw^2(2\delta+h)}{\delta(\delta+h)+w^2} + w^2 - 4x^2}}\right)} \tag{2.1}$$

The equation relating a the number of sides of an n-sided regular polygon with the edge length, h, and effective radius, r is given by Equation 2.2, below. A complete derivation can be found in Appendix B.

$$n = \frac{\pi}{\sin^{-1}\left(\frac{h}{2r}\right)} \tag{2.2}$$

Comparing Equation 2.1 to Equation 2.2, it can be seen that the radius of the deformable wheel can be expressed as Equation B.16.

$$r = \frac{1}{2}\sqrt{-\frac{h^2w^2\left(\delta h + w^2\right)}{\left(\delta(\delta+h)+w^2\right)^2} + h^2 + \frac{hw^2(2\delta+h)}{\delta(\delta+h)+w^2} + w^2 - 4x^2} \tag{2.3}$$

To validate Equation 2.3, three wheels were folded with various design parameters and the diameters of the wheels were measured with calipers at various axial deformations. The measured data was plotted against the Equation 2.3 model and is shown in Figure 2.5. In all three cases, the models closely matched the measured diameters. From these tests, it was determined that the n-sided regular polygon approximation was a reasonable model for the behavior of the deformable wheel.

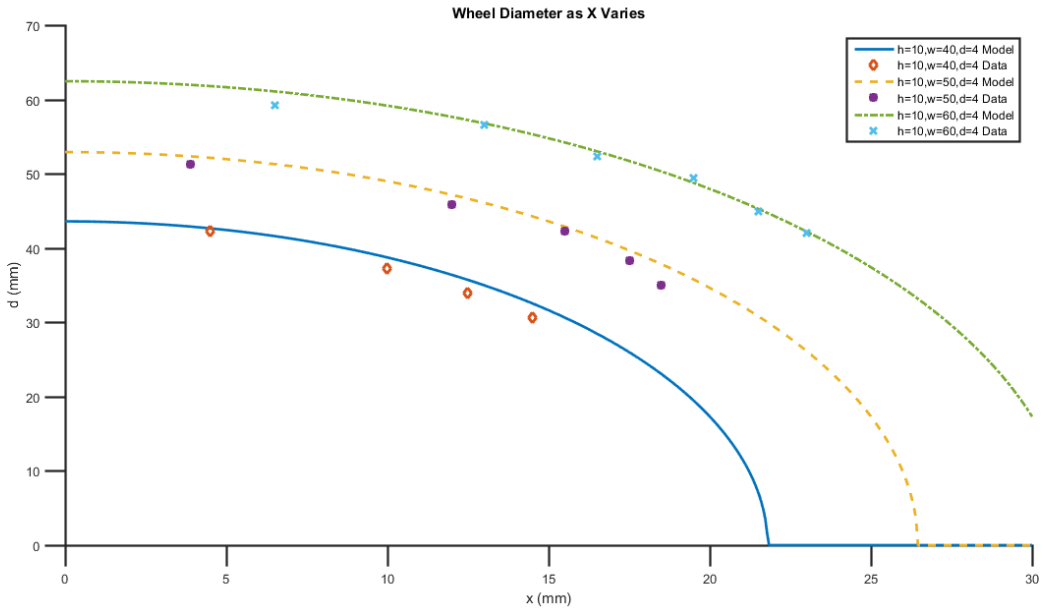

Figure 2.5: Equation 2.3 Plotted Against Measured Data

2.3 Optimization of Wheel Deformation

As discussed later in Chapter 4, maximizing the total deformation of a wheel is highly desirable. The performance of the steering, transmission, and suspension increase proportional to the maximum change in radius of the deformable wheel.

The Benyon spring has a finite radial deformation; when the spring is being expanded there exists a critical point where further deformation is not possible. A rigorous mathematical proof of where this critical point exists was not obtained. However, an approximation was obtained via observation. During the folding process, the wheel is 'folded under' itself, as shown in Figure 2.6. The 'fold under' creates an outer sheath for the wheel to spiral into. It is believed that this phenomenon only exists for material with thickness; a computer model with zero thickness did not

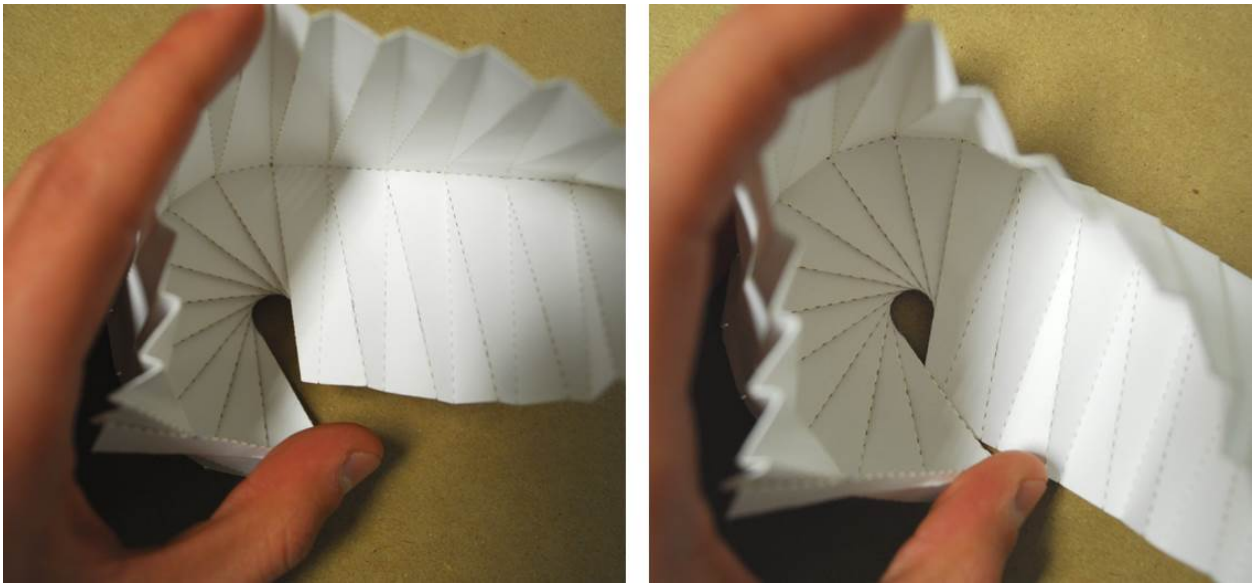

Figure 2.6: 'Critical' Folding Step

exhibit the sheathing behavior. From observation, the number of sections that had been folded immediately after the 'fold under' was the number of sides of the n-sided approximating polygon when the wheel was fully deformed. For example, in Figure 2.6, the twelfth fold was the 'fold under' step. When fully deformed, the wheel would form a 12-sided regular polygon.

The critical fold point was approximated by Figure 2.7. The number of sides, n', at the critical point is described by Equation 2.4 which is derived fully in Appendix B. Both θ and α are functions of the three design parameters. Knowing the minimum number of sides in terms of the design parameters allowed the minimum radius, r', to be found using Equation 2.2.

$$n' = \frac{\pi + \theta}{2\alpha} \tag{2.4}$$

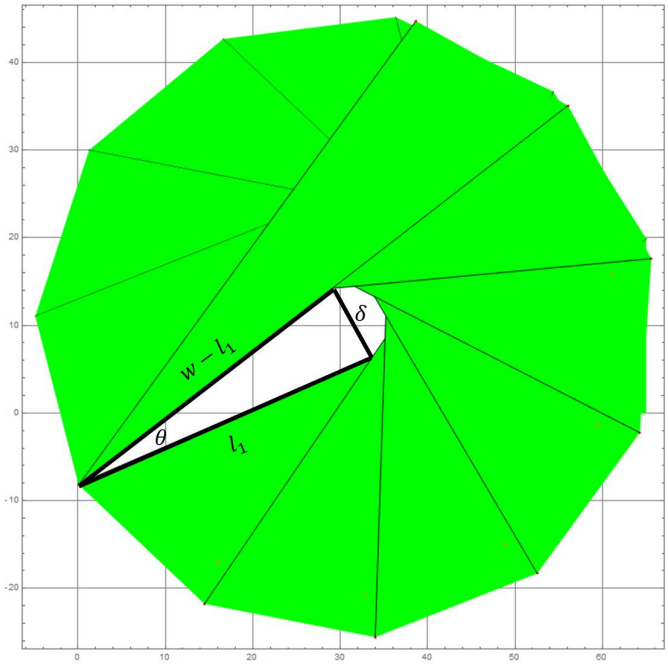

Figure 2.7: Approximation of the Wheel at the 'Critical Fold' Step

Dividing the minimum radius, r', by the original radius, r_0, results in the deformation ratio, η, which is expressed in Equation 2.5 and derived in Appendix B. The ideal wheel design minimizes the deformation ratio.

$$\eta = \frac{r'}{r_0} = \frac{\sin(\alpha)}{\sin\left(\frac{2\pi}{\pi + \theta + 1}\right)} \tag{2.5}$$

Both α and θ depend on the three design parameters, h, w, and δ. When fully expanded, Equation 2.5 does not provide clear insight to the relationship between the design parameters and the deformation ratio. Multiple trigonometric functions obscure how changing one parameter affects the deformation ratio. Furthermore, η is a function of three variables and is not easily visualized. To help offer insight into the function, δ was assumed to be fixed since it is the physical shaft size the wheel

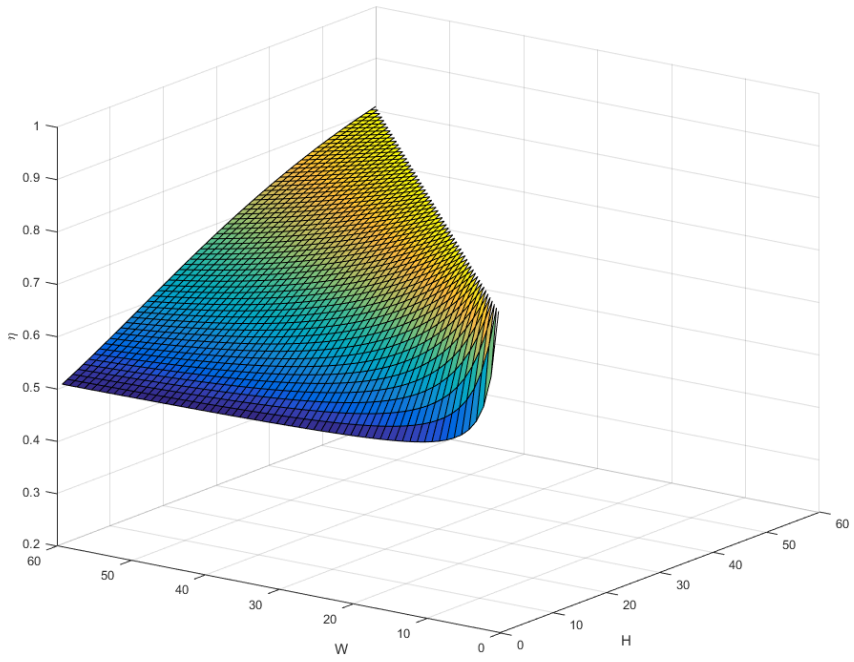

Figure 2.8: Deformation Ratio as h and w Varied for a Constant $\delta = 0$

needs to fit. Making the assumption that δ is a constant reduces η to a function of two variables which can be easily visualized, as shown in Figure 2.8. The percentage of radial deformation was plotted as a function of only h and w with $\delta = 0$. From the plot, several conclusions were drawn about the effects of h and w on the deformation ratio. Generally, as h decreases, the deformation ratio decreases and as a w increases, the deformation ratio decreases. Numerical solvers were used to determine that has h approaches 0 and w approaches infinity, the deformation ratio approaches 0.50. In the inverse case, as h grows and w approaches 0, the deformation ratio approaches 0.80.

Setting δ to a non zero constant introduced an interesting feature in the deformation ratio plot; a valley appeared which provided a local minimum for the deformation ratio. When $\delta = 0$, the deformation ratio plot was completely convex but with the introduction of δ, new curvature was introduced. There exists a combination of δ, h, and w which locally minimizes the deformation ratio. An analytic function to approximate the valley in terms of the design parameters was not obtained. Another important feature of the graph is that the overall deformation ratio was increased by adding δ. In Figure 2.8, the deformation ratio at $h = 0, w = 60$ is near 0.5, but, in Figure 2.9, the equivalent deformation ratio is closer to 0.6. However, when η was numerically computed as h approaches 0 and w approaches infinity, the deformation ratio approached 0.5. Additional spikes in the deformation ratio plot appeared for physically trivial cases, such as when δ was greater than h and w, which is physically impossible to fold.

From the plots of the deformation ratio, without constraints, the ideal deformable wheel pattern minimizes h and δ while maximizing w.

The theoretically computed values of the deformation ratio are compared with measured values in Table 2.1, below. Diameters of deformed folded wheels were measured with calipers and compared to the undeformed original diameters to determine the experimental deformation ratio.

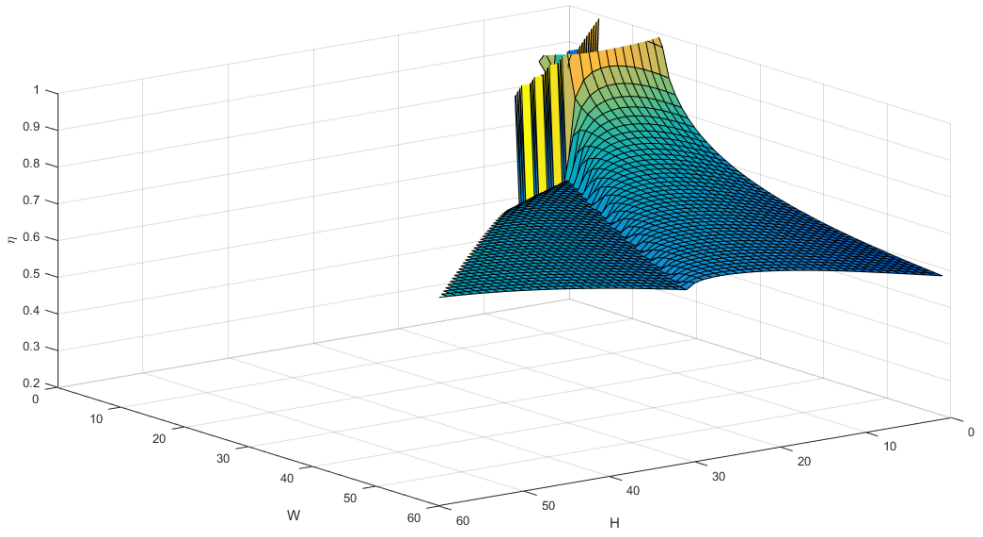

Figure 2.9: Deformation Ratio as h and w Varied for a Constant $\delta = 7.9375$ (5/16")

Table 2.1: Theoretical and Experimental Deformation Ratios

Design Parameters (mm)					
h	w	δ	Theoretical η	Experimental η	% Difference
10	40	0	0.5897	0.5732	2.7
10	40	4.7	0.6526	0.6359	2.5
10	50	4.7	0.6244	0.6232	0.2
10	60	4.7	0.6045	0.6062	0.3
15	75	7.9	0.6314	0.6465	2.3
20	40	4.7	0.6696	0.6576	1.7

Chapter 3: Creation of Foldable Laminate

Two manufacturing methods were attempted to develop a material suitable for prototyping origami mechanisms. First, Shape Deposition Manufacturing (SDM) was attempted and it was found that the method did not scale to large origami designs. After some trial and error, a novel method using 3D printing was developed to fabricate an origami material. The 3D printed method was then compared in load tests with paper and polyester.

For both the SDM and 3D printing methods, it was desired to attach rigid sections to a polyester flexure. A model of a single fold joint with rigid pieces on the top and bottom side of the flexure can be seen in Figure 3.1. The maximum fold angle is given by Equation 3.1. Optimally, θ is as close to 0 as possible meaning the joint can completely fold over. To minimize θ, δ and α should be maximized while t should be minimized. The thickness and angle of the rigid layer are limited by the process used to fabricate the material.

$$\theta = \tan^{-1}\left(\frac{t}{\delta \cot \alpha}\right) \tag{3.1}$$

θ Fold Angle
δ Rigid Offset
t Thickness of Rigid Layer
α Angle of Rigid Layer

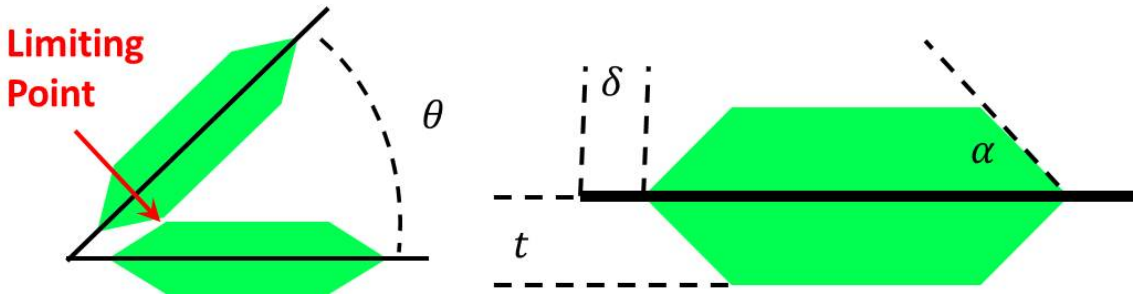

Figure 3.1: Fold Angle Limitations

If the rigid material is only one side of the flexure, then θ is 0 in one direction while limited by Equation 3.1 in the other direction. For example, if the rigid material is only placed on the top side of the flexure, the joint can theoretically fold inward completely. However, the folding the joint up will cause the rigid material to contact and limit the fold angle.

For both the SDM and 3D printing methods, a C# Solidworks macro was written to generate the necessary manufacturing files. The macro required a geometric unit specified as a series of lines, how many times the unit should be repeated in the design, and how much the solid regions should be offset from the fold lines. The macro then generated DXF files for laser cutting and STL files to 3D print or generate CAM profiles.

3.1 Shape Deposition Manufacturing

Shape Deposition Manufacturing (SDM) is the process of iteratively casting and milling to create multi-material parts [5]. Two materials commonly used with SDM are urethane, a two part epoxy that cures to a hard and brittle state, and silicone rubber which is pliable when cured. In general, a cavity is milled in a sacrificial block,

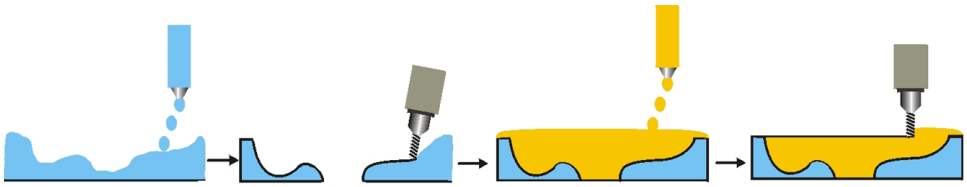

Figure 3.2: Diagram of the Iterative Milling and Casting of the SDM Process [26]

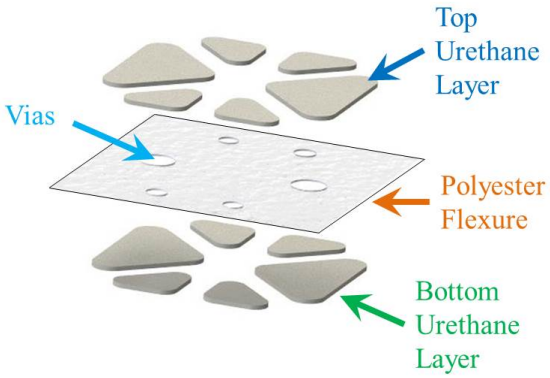

Figure 3.3: Desired SDM Outcome for Origami Material

often made of wax, and filled with urethane. After the urethane cures, a new cavity is milled and filled with silicone. A visualization of the SDM process can be seen in Figure 3.2.

3.1.1 Manufacturing Process

To use Shape Deposition Manufacturing to produce a material suitable for origami, it was desired to adhere rigid sections of urethane to a polyester flexure. A CAD rendering of the desired outcome is shown in Figure 3.3. Sections of urethane are on the top and bottom of a polyester flexure and are connected with vias through the polyester flexure. After initial testing, it was determined that urethane does not bond

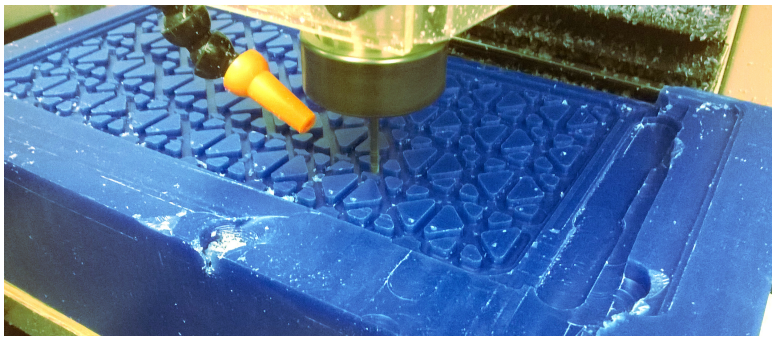

Figure 3.4: Wax Mold Negative Being Milled

with polyester and will flake off; however, the vias allow the two layers of urethane to form a single entity that is not removable.

A visualization of the SDM process for a single 'water bomb' fold pattern is available in Figure C.1 of Appendix C. First a large cavity was milled in a wax block to contain excess urethane from subsequent steps. Then, the negative of the rigid sections for the 'water bomb' were milled in the bottom of the cavity. The result of these two operations is shown in the first segment of Figure C.1. The cavity was then filled with Smooth-On^{TM} Task-9 urethane which was allowed to cure overnight. The urethane was milled away leaving a 0.5 mm layer in the negative, shown in the third section of Figure C.1. The vias and fold lines were laser cut in a polyester flexure which was then placed on top of the bottom layer of urethane. The wax block was removed from the CNC mill and replaced with a new wax block.

Initially, a solid layer of urethane was poured and then areas where folds were desired was milled down to the polyester flexure. However, the CNC mill used was not capable of milling the urethane away accurately, the polyester flexure was often punctured in the milling process. To eliminate the need to mill on the fold lines, a

Figure 3.5: Completed SDM Water Bomb Segment

wax mold was created to contain the urethane for the top layer pour. The wax mold ensured that urethane only cured in areas where a rigid section was desired. The wax mold prevents the need to mill to the surface of the polyester flexure since the wax mold can be peeled away, leaving the top layer of urethane behind and exposing the fold lines in the flexure. A negative for the wax mold, shown in Figure 3.4 was milled in the new wax block 10 mm deep and filled with melted wax shavings. The wax mold was then removed from the cavity and placed on top of the flexure, as shown in the center panel of Figure C.1. The original sacrifical wax block was then placed back on the mill. To reduce the error introduced by removing the original block from the mill and to reduce machining time, the wax mold could have been milled and poured first.

After the wax mold for the top layer was placed, the top layer of urethane was poured, and after curing, milled to 0.5 mm thickness. The finished piece was then removed from the mold and can be seen in Figure 3.5.

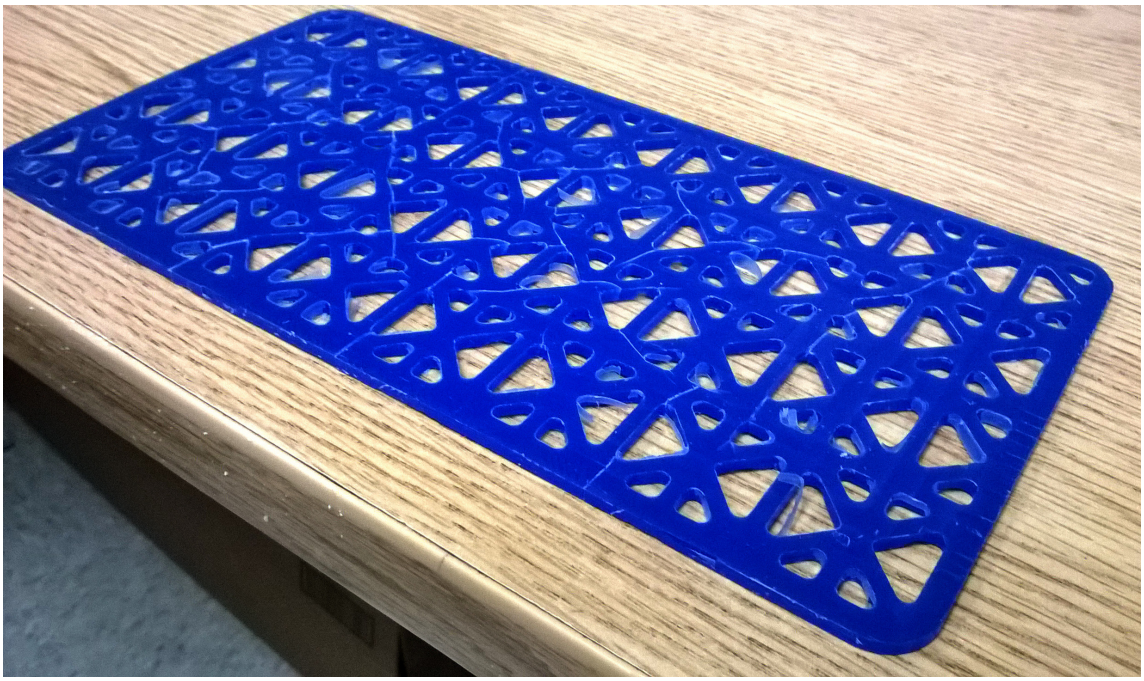

Figure 3.6: Cracking in Wax Mold From Uneven Thermal Stresses While Cooling

3.1.2 Limitations

The Shape Deposition Manufacturing process worked well for a single 'water bomb' unit. However, when used for the entire 'magic ball' pattern [15], the process did not scale. The wax guide isolating the top urethane layer consistently cooled unevenly, causing it to crack, shown in Figure 3.6. For a single unit, the wax did not crack while cooling. The poured urethane entered the cracks, causing the wax guide to float, which allowed a solid layer of urethane to form on the flexure. The solid layer of urethane prevented the polyester flexure from bending. A successful 'magic ball' origami wheel was not produced with SDM and was not pursued further after three failed attempts.

The SDM process was also time consuming; the full 'magic ball' pattern required 23 hours of CNC machine time. The length of time required to prototype an origami mechanism using SDM is not ideal for an iterative design process. Additionally, urethane casting is a toxic process. Urethane releases toxic fumes while it cures and the uncured polymer is a highly flammable skin irritant [28].

3.2 Fused Deposition Modeling 3D Printing

Fused Deposition Modeling (FDM) 3D Printing is the process of building up layers of extruded material into a 3D solid. Fused Deposition Modeling 3D printing has recently seen wide adoption due to the low cost open source RepRap and commerical Makerbot 3D printers which convert 3D geometry in the form of STL files to physical 3D objects [17, 22].

3.2.1 Manufacturing Process

Similar to the SDM process, the goal of the 3D printed manufacturing process was to adhere rigid material to a polyester flexure. A Makerbot Replicator 2X printing ABS plastic was used to fabricate the material.

Initially, printing ABS plastic directly onto the polyester flexure was attempted. However, similar to the urethane, the ABS would fall off the polyester. Vias were once again used to attempt to get the top and bottom layers to adhere to one another. The top layer was printed on the polyester, the workpiece was flipped, and then the bottom layer was printed. However, the bottom layer extrusions did not fall or flow into the vias, instead the two pieces of ABS remained separated.

To help the ABS adhere to the polyester, a layer of polyimide (Kapton^{TM}) tape was applied to the polyester. Polyimide is used in most 3D printers to help ABS stick

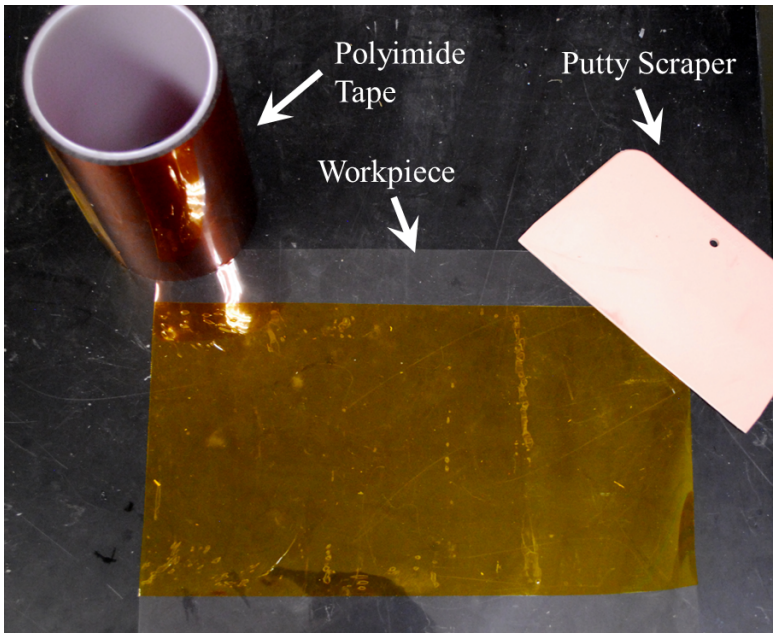

Figure 3.7: Polyimide Tape Placed on Polyester Sheet

to the build plate while printing. At first, the polyimide tape appeared to prevent the ABS from flaking off. However, when folding the origami patterns, the ABS would pop off the polyimide.

Some hobbyist 3D printing enthusiasts recommend using an 'ABS glue' to help printed objects stick to the build plate [6]. ABS glue is made by dissolving ABS plastic in acetone to form a slurry. When the ABS glue is applied to a surface, the acetone evaporates, leaving behind a thin layer of ABS plastic. ABS plastic adheres well to ABS plastic, helping prints stick to build plates. This process was used to help adhere the 3D printed rigid sections to the polyester/polyimide workpiece. Since the ABS plastic adhered to the ABS glue, the vias were not used and rigid material was only printed on one side of the workpiece.

Figure 3.8: Polyester/Polyimide Workpiece After Laser Cutting the Fold Pattern

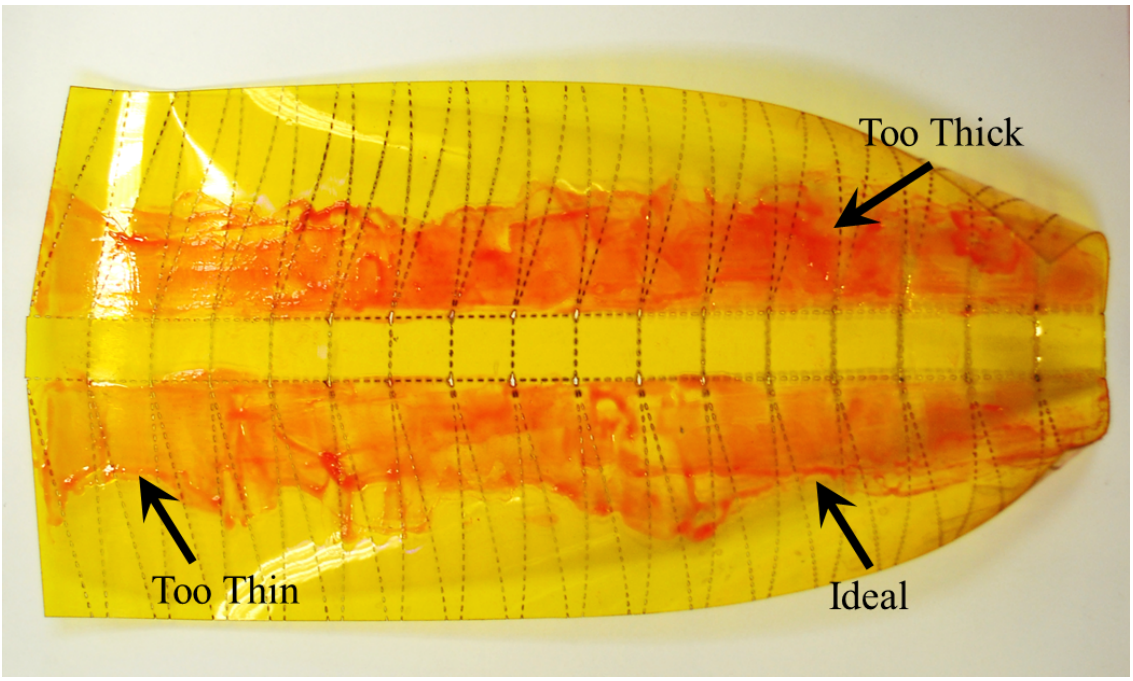

Figure 3.9: Thin, Ideal, and Thick Sections of ABS Glue

The first step in the manufacturing process was to stick a layer of 0.05mm polyimide tape on the polyester sheet. Bubbles that formed between the polyimide and the polyester were pushed to the edge of the workpiece with a putty scraper, shown in Figure 3.7. The desired fold pattern was then perforated in the polyester/polyimide workpiece using a laser cutter; the perforated workpiece can be seen in Figure 3.8. Burnt residue from the laser cutter was cleaned from the workpiece using isopropyl alcohol. An ABS glue mixture was then painted onto the regions of the workpiece that would have rigid sections printed on them. The ABS glue was made from dissolving failed prints in acetone. As acetone evaporated from the mixture, more acetone was added to keep the glue at the consistentcy of uncrystallized honey. The glue was spread on the polyimide side of the workpiece until a thin but opaque layer of ABS

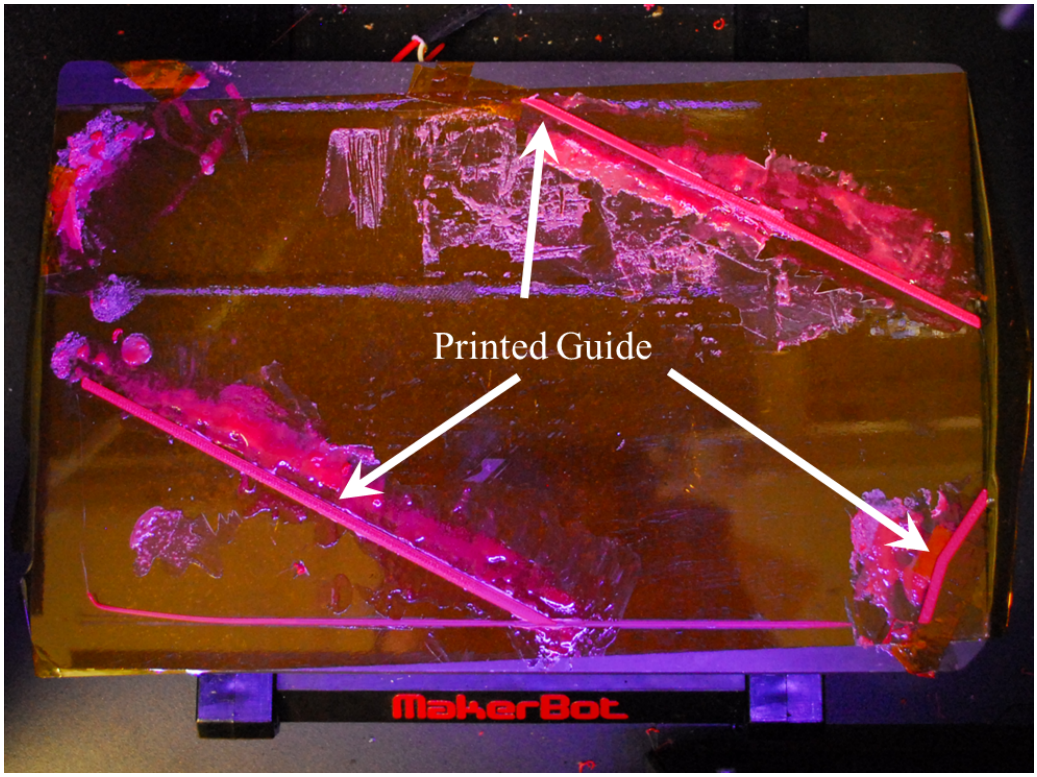

Figure 3.10: Alignment Guide Printed on Build Plate

was deposited; an ideal glue layer is shown in Figure 3.9. If the glue was too thin, the ABS did not adhere properly when printed and if the glue was too thick, the printer nozzle would clog when printing. While the glue was drying, a guide was printed on the Makerbot and left on the build platform.

The guide, shown in Figure 3.10 was used to align the workpiece on the build plate. The outer perimeter of the workpiece was printed, and then the polyester sheet was taped inside of the guide with the polyimide/ABS glue side up. In the 3D printer configuration software, the guide and the 3D printed layer had the same coordinates and rotation angle which was selected to maximize the total printable area of the Makerbot.

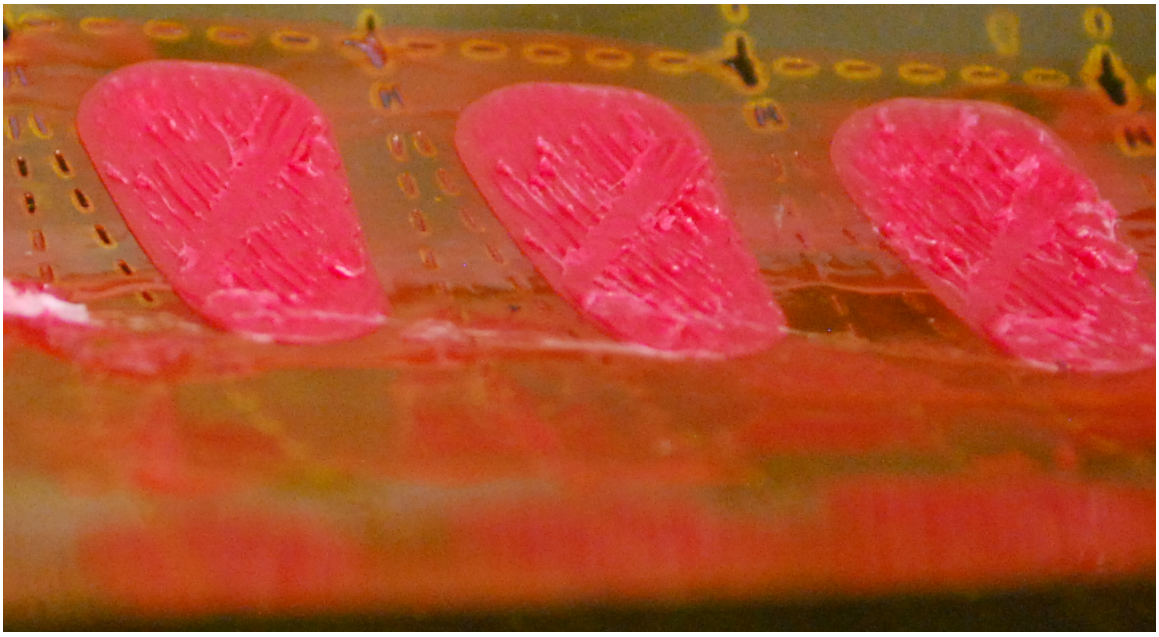

Figure 3.11: Detailed View of the 3D Printed Layer

After the workpiece was taped to the build plate, the layer of ABS was printed. A custom profile for the Makerbot was created using ProfTweak [21]. The custom profile set the Makerbot to print with a 0.3mm layer height and an approximate extrusion width of 0.75mm. The extrusion width was increased from the standard size to reduce the number of passes required to create a rigid section. In practice, the 3D printed layer was 0.45mm thick. The 3D printed sections were offset from the fold lines by 4 mm which allowed for some error in positioning the material and improved the maximum attainable fold angle described in Equation 3.1. A close-up view of a 3D printed segment can be seen in Figure 3.11 and the folded 3D printed wheel can be seen in Figure 3.12.

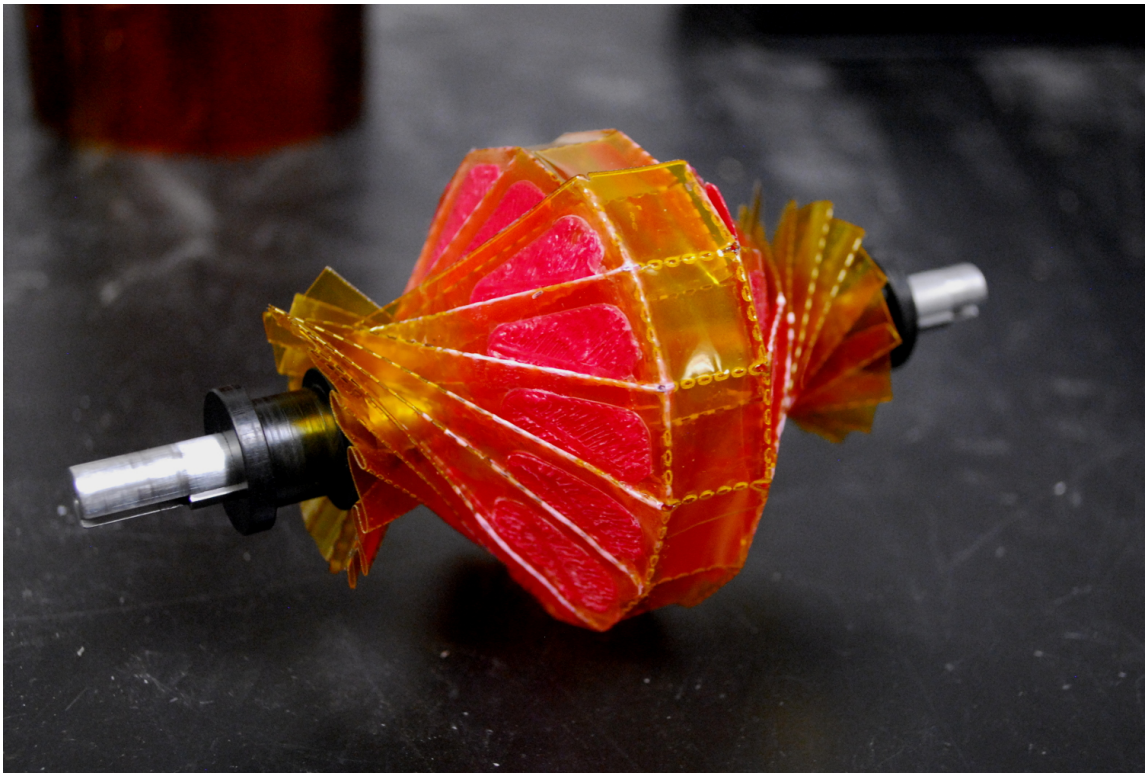

Figure 3.12: Folded 3D Printed Wheel

3.2.2 Limitations

The main limitation with the 3D printed method is the limited size of fold pattern that can be produced. The regions of ABS plastic are constrained by the size of the 3D printer used. Additionally, the ABS sections can be removed from the workpiece, even when ABS glue is used, if significant force is applied underneath the ABS piece. A remedy for this was to run the workpiece through a hot roll laminator prior to folding. The laminator placed two pieces of hot melt plastic on either side of the workpiece and partially compressed the 3D printed sections. However, the additional layers of plastic increased the energy required to fold and later actuate the mechanism. The actuation force required was too high for the actuator described in Section 4.1 so the lamination step was omitted from the process. Another limitation of the 3D printed method is the accuracy. The workpiece is placed in the 3D printer by hand and may not be aligned properly. Similarly, the process relies on ABS glue which is created and applied in an objective manner. Due to the evaporative nature of acetone, a clear 'recipe' for the glue does not exist; the proper viscosity is subjective and was determined through trial and error.

3.3 Wheel Load Testing

3.3.1 Experimental Methodology

Deformable wheels made of paper, polyester, and the 3D printed laminate were tested for load bearing capacity. Due to the scalability issues of the SDM manufacturing process described in Section 3.1, SDM wheels were not tested. The paper and polyester wheels were laser cut and folded carefully. If an in-plane section became deformed during the folding process, the wheel was not tested. The paper wheels were

folded from 0.19mm thick 90lb cardstock. The polyester wheels were folded from 0.10mm thick polyester transparency sheets. A summary of the material properties of the paper and polyester tested can be seen in Table 3.1. The 3D printed wheels were manufactured with the 3D printed method described in Section 3.2. After folding, each wheel was actuated one time by hand to ensure operability and then stored in a fully compressed state until tested.

Table 3.1: Summary of Material Properties

	Paper [11]	Polyester (20 °C)[8]
Young's Modulus (GPa)	2.14	3.5
Density (kg/cm^3)	0.865	1.390

Four wheels of each material were placed on the chassis described in Chapter 4. The chassis was placed on blocks to prevent the wheels already mounted on the chassis from experiencing loads while additional wheels were attached. Prior to mounting, the axles were thoroughly cleaned of grease and dried to prevent damage to the paper wheels. After the wheels were mounted, the servo actuators described in Section 4.1 were set for a distance of 25.40 mm.

After all four wheels were on the chassis and the servo actuators were set, the chassis was placed on a flat table. Mass was slowly added to the chassis in 5g increments until a single wheel yielded. The current mass loading was recorded. Mass continued to be added to the chassis until a single wheel failed. Yielding was visibly distinct and was defined as a deformation that would prevent the wheel from functioning, an example of yielding is shown in Figure 3.13. Failure was defined as a catastrophic

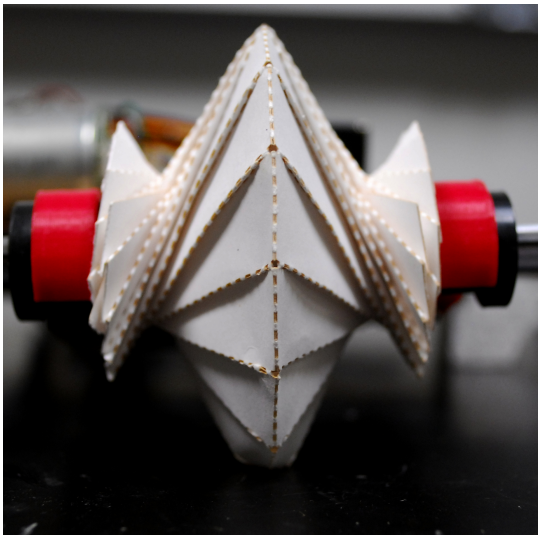

Figure 3.13: Example of Yielding

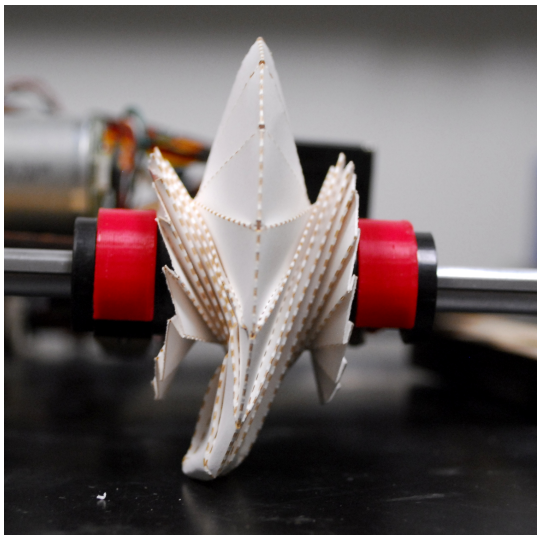

Figure 3.14: Example of Failure

collapse of a wheel and can be seen in Figure 3.14. Both yielding and failure occurred instantaneously. Yielding was visibly distinct and caused a slight shifting in the chassis. Wheel failure caused the entire chassis to become unsupported and fall down.

Five sets of wheels made of paper and polyester were tested. Three sets of the 3D printed wheels were tested.

3.3.2 Load Testing Results

The load testing results for the paper, polyester, and 3D printed wheels can be seen in Table D.1, Table D.2, and Table D.3, respectively, in Appendix D. A summary of the results are presented below in Table 3.2 and Figure 3.15. All loads reported are the loads carried by all four wheels. The load on an individual wheel is the reported load divided by four. Dividing the applied load is only a fair metric for the first

wheel to yield. Once a single wheel yielded, the loads carried by the remaining three unyielding wheels were indeterminate.

Table 3.2: Summary of Load Testing Results

	Paper Wheel	Polyester Wheel	3D Printed Wheel
Average Yield Load(N)	11.976	24.708	76.907
Yield Load Standard Deviation (N)	0.041	2.660	1.663
95% Confidence Interval (N)	[11.89 12.05]	[19.35 30.06]	[72.99 80.82]

The average yield load for the paper wheels was 11.976 N with a standard deviation of 0.041 N. The 95% confidence interval for the true mean was [11.89 12.05] N. The polyester wheels had an average yield load of 24.708 N with a standard deviation of 2.660 N resulting in a 95% confidence interval of [19.35 30.06] N. The 3D printed wheels had an average yield load of 76.907 N and a 95% confidence interval of [72.99 80.82] N.

After the wheels failed the distance between the servo actuator was measured. In all cases the distance remained 25.40 mm.

3.3.3 Analysis of Results

The true mean of the 3D Printed material was 2.42-4.18 times higher than polyester, and 6.05-6.80 times higher than paper. Using buckling as the failure criteria, it was expected that the 3D printed material would be several orders of magnitude stronger than the polyester.

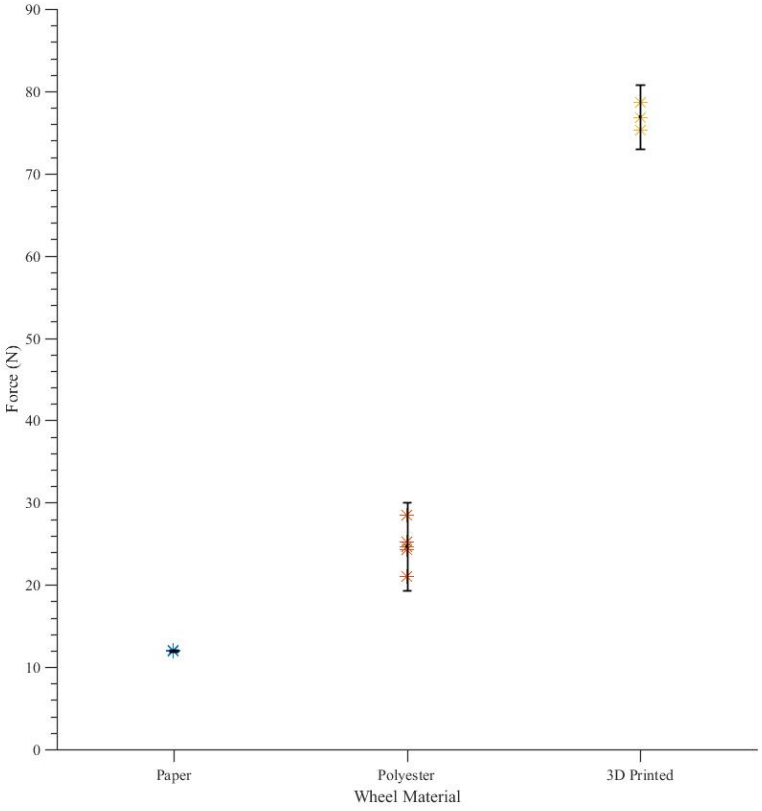

Figure 3.15: Comparison of Yield Loads With 95% Confidence Intervals

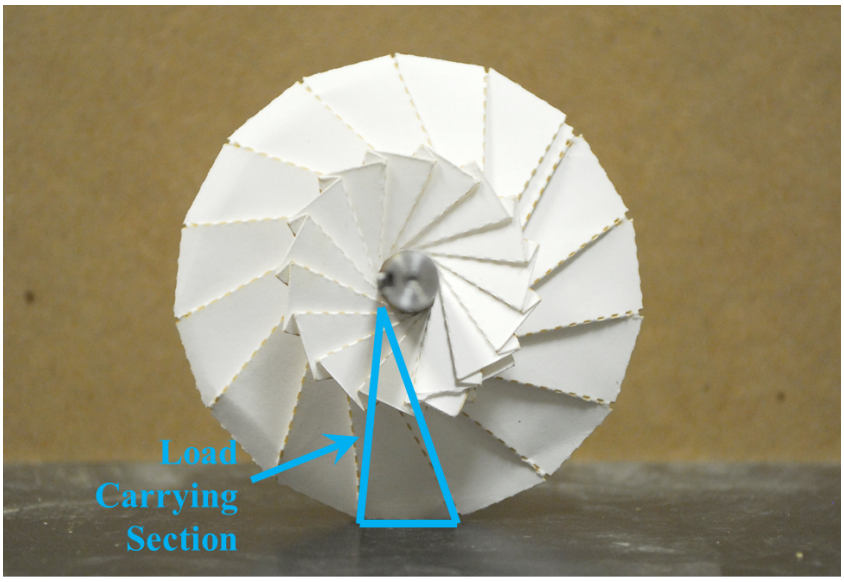

Figure 3.16: Load Carrying Section of Wheel

When the wheel is in contact with a surface, a single segment carries the majority of the load and is highlighted in Figure 3.16. The segment was analyzed as a nonuniform beam with a linearly varying moment of inertia. The critical load for buckling of beams with linearly varying moments of inertia is given by Equation 3.2 [19].

$$P_{cr} = \frac{EI}{L^2}\lambda \tag{3.2}$$

P_{cr}	Critical buckling load
E	Young's Modulus
I	Largest Moment of Inertia
L	Length
λ	Normalized Loading Constant

For all materials tested, I, L, and λ remained constant; only E changed from material to material. The Young's Modulus of polyester was 1.63 times larger than that of the paper tested, thus it was expected the polyester wheels would carry approximately 1.63 times the load; the true mean of the polyester yield load was 1.6

to 2.5 times larger than that of paper. To compare the paper and polyester wheels to the 3D printed wheels required finding an equivalent area moment of inertia for the 3D wheel. Treating the 3D printed material as a composite made from polyester, polyimide, and ABS, the equivalent area of moment of inertia was found using standard laminate methods. Polyester was used as the base material when calculating $A*$, the equivalent area, using Equation 3.3 [9]. Detailed calculations for the laminate moment of inertia can be found in Appendix B. For the analysis, ABS was treated as an isotropic material. However, 3D printed structures are anisotropic; each 3D print is uniquely anisotropic and the g-code used to generate the print must be analyzed to determine the material properties, which was deemed out of the scope of this research [27]. The overall moment of inertia for the 3D printed laminate was found to be 10^5 times larger than that of the plain polyester wheel. Thus, it was expected that the 3D printed wheel would have carried roughly 10^5 times more load than the polyster wheels which did not happen during the experiment.

$$A^* = \frac{E_{poly}}{E} tw \tag{3.3}$$

A^*	Effective Area
E	Young's Modulus of Non Polyester Material
t	Layer Thickness
w	Layer Width

A critical assumption in treating the 3D printed wheel as a laminate was that the 3D printed ABS extended to the edge of the load bearing section. As described in the Section 3.2, the ABS plastic was offset 4mm from the folds. Unlike the paper and polyster wheels, the 3D printed wheel did not fail from buckling; the region of polyester/polyimide folded beneath the wheel as shown in Figure 3.17.

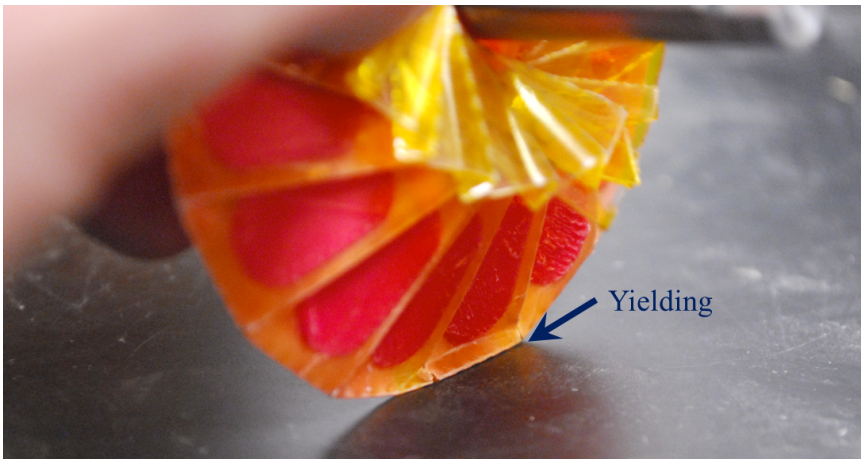

Figure 3.17: Yielding of 3D Printed Wheel

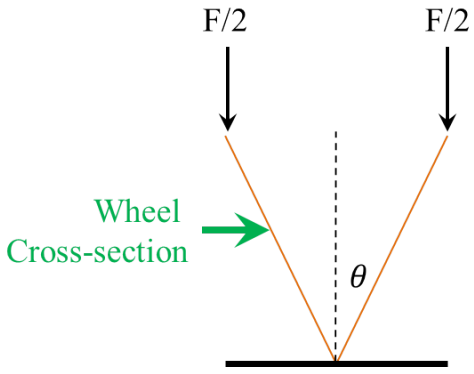

Figure 3.18: Free Body Diagram of Wheel

The failure of the wheel was modeled as yielding of the polyester/polyimide layer. The free body diagram of the scenario can be seen in Figure 3.18 where F was the load on the axle. The applied load was carried evenly by two segments of the wheel, shown in orange in Figure 3.18. The stress in the flexure was given by Equation 3.4.

$$\sigma = \frac{F}{A} + \frac{Mc}{I} \tag{3.4}$$

σ	Stress
F	Applied Force
A	Cross Sectional Area
M	Applied Moment
c	Distance From Bending Axis
I	Area Moment of Inertia

The average yielding load for the 3D printed wheel was 11.97N, which caused approximately 100 MPa of stress in the wheel, detailed calculations are given in Appendix B. The yield stress of polyester was approximately 83 MPa and the yield stress of the polyimide is approximately 138 MPa [8, 7]. Treating the laminate as a composite with a polyester matrix and polyimide fibers, the weighted average by volume fraction of the yield strengths is approximately 100 MPa, which coincides with the experimental yield load; detailed calculations are provided in Appendix B.

To eliminate the yielding failure case, the 3D printed ABS section could extend to the fold edges. Expanding the ABS region reduces the margin for error in aligning the material on the 3D print bed and reduces the fold angle of the joint in one direction, both of which are undesirable.

Chapter 4: Design of a Prototype Chassis

To demonstrate that a deformable wheel could function as the suspension, transmission, and steering of a vehicle, a small proof-of-concept robot was built and is described in Section 4.1. A commercial robotics driver did not exist that met the requirements for the robot, so a custom robot controller was built and is described in Section 4.2.

4.1 Chassis Design

The chassis was primarily made from laser cut 1/4" birch plywood and had an overall mass of 0.914 kg. The vehicle also had laser cut acrylic gear trains and 3D printed ABS bushings.

The chassis consists of four repeated units. Each unit contains a DC motor, a compound gear train, a deformable wheel, and an actuator driven by a high torque servo motor. A single unit can be seen in Figure 4.2. The DC motors were salvaged from iRobot Roomba 500 series robotic vacuums. The motors were low cost, included an encoder, and met the voltage and torque requirements. The DC motor powered a laser cut acrylic gear train, which was designed to have an overall ratio of 31:1. The encoders on the Roomba motors generated a square wave with four pulses per revolution, so the gear ratio was designed for the encoder to generate an integer

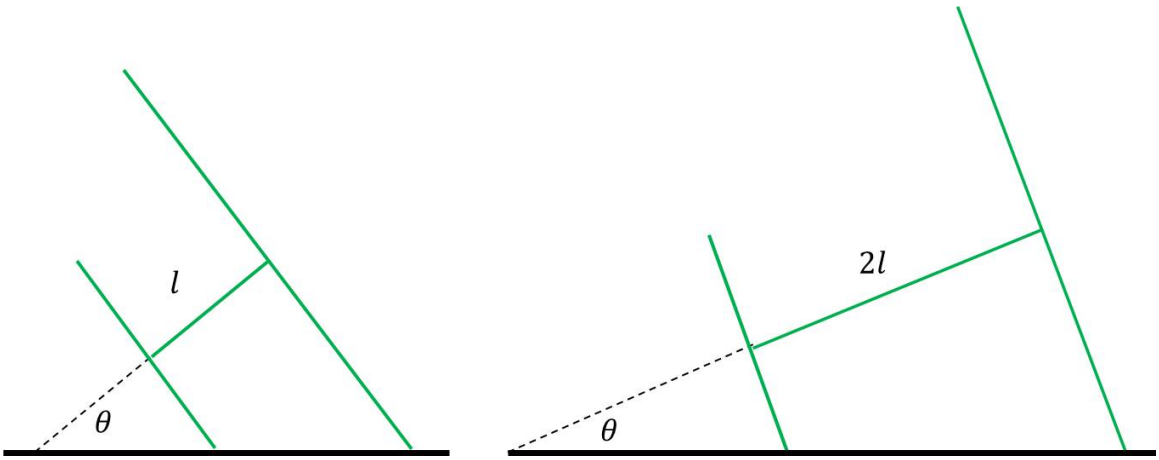

Figure 4.1: Comparison of Tilt Angle for Different Chassis Sizes

number of pulses for a complete revolution of the wheel. A Python script was written to iterate over various numbers of gear teeth until an optimal overall ratio was found. The gear train then drove keyed 5/16" diameter aluminum shaft to which the wheel was attached.

There were four primary goals when designing the chassis. To maximize effectiveness of the deforming wheels, the distance between the wheels needed to be minimized. To reduce the force required to deform the wheel, overall weight of the robot was considered. The actuation mechanism also needed to be able to slide along the shaft while being rotated. Additionally, the wheels needed to deformed.

One of the driving design goals for the chassis was to minimize the distance between the contact lines of the deformable wheels. With the contact lines closer together, the chassis can overcome larger obstacles than if the center lines are farther apart, as shown in Figure 4.1. The limiting factor in keeping the contact lines close was that decreasing the radius of the wheel requires significant axial deformation. In

order to decrease the radius of the wheel to 6.3 cm, the wheel had to axially deform 3.0 cm. The total distance between the front wheels on the chassis was 12.5 cm, allowing the chassis to reach a total tilt angle of 9.0 degrees. The relationship between total tilt, wheel deformation, and centerline distance is characterized by Equation 4.1. In a best case scenario, the vehicle is able to overcome obstacles 2.0 cm in height and still maintain a level platform.

$$\theta = \tan^{-1}\left(\frac{\delta}{l}\right) \tag{4.1}$$

θ maximum platform angle
δ maximum change in wheel radius
l distances between wheel centers

Another design goal was to minimize the weight of the chassis. Birch plywood was chosen as the main material because it met the load requirements and was lighter than other common laser cut materials such as acrylic. Extraneous material was removed from the design to reduce weight, leading to the curved profiles of the side rails of the robot. Additionally, PTFE coated bushings were used to mount the axles to the chassis instead of heavier ball or roller bearings. Aluminum axles were used in part to save weight, and in part to ease machinability.

To achieve sliding and rotating motion, a keyed shaft was used. A spring steel key was mounted the entire length of the shaft. A delrin bushing then rode on the key, as seen in Figure 4.2. The deformable wheel was attached to the delrin bushing with M2 machine screws. The key allowed the delrin bushing to slide along the shaft while also being rotated. The sliding and rotating motion of the delrin bushing was critical for the wheel to be deformed while still being driven. The delrin bushing

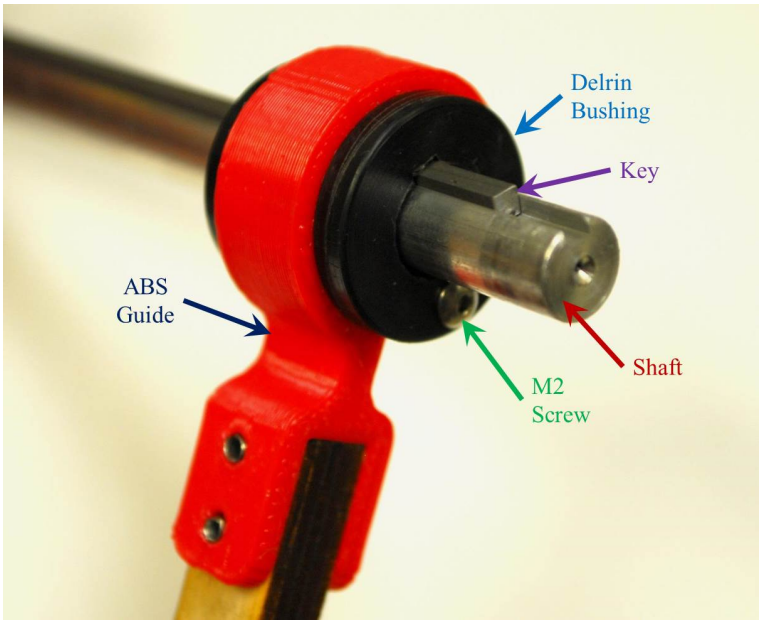

Figure 4.2: Sliding and Rotating Bushing

was attached to the actuation mechanism with 3D printed arms. The arms rode in a groove in the top of the bushing and pushed the delrin axially to deform the wheel. The delrin bushing can rotate freely in the ABS guide.

Symmetric actuation was accomplished through a rack and pinion mechanism, shown in Figure 4.3. A HiTec-422SB high torque servo motor was used to drive the actuator mechanism. Two rack gears were placed on opposite sides of the pinion gear, causing them to move equal and opposite distances. The pitch diameter of the pinion gear was selected to be 3.175 cm, allowing 0.027 cm of rack gear travel per degree of rotation. Since the rack gears move equally and opposite, each degree of rotation causes the wheel to expand or contract by 0.055 cm. Increasing the radius of the pinion gear would increase the resolution of the actuation mechanism but in exchange the torque required to compress the wheel would increase.

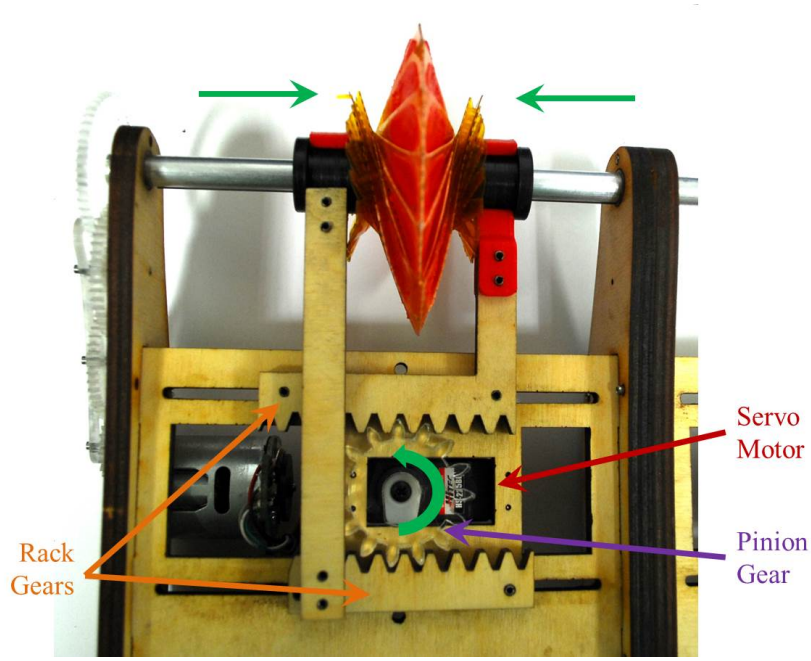

Figure 4.3: Symmetric Actuation Mechanism

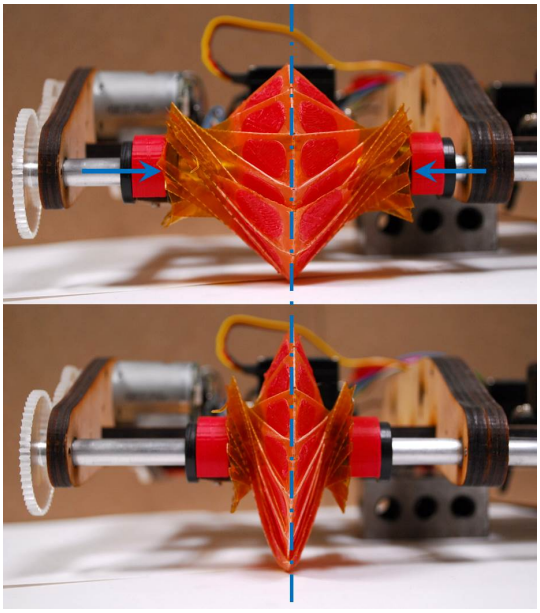

Figure 4.4: Symmetric Actuation of the Wheel

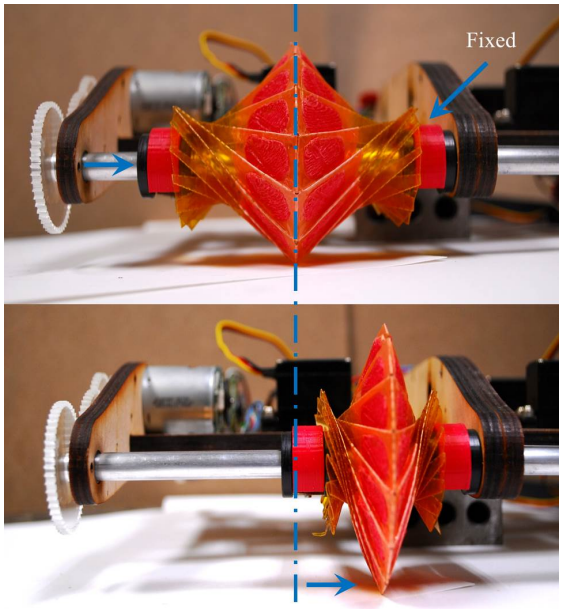

Figure 4.5: Asymmetric Acutation with the Right Side Fixed

If the wheel was not actuated symmetrically, the wheel edge would be moved across the ground. A comparison of non-symmetric and symmetric actuation can be seen in Figures 4.4 and 4.5. In Figure 4.5 the centerline and surface contact position of the wheel stays constant while being actuated. When the wheel undergoes asymmetric actuation, shown in Figure 4.5, the centerline and contact position of the wheels move to the right. Sliding the contact surface across the ground induces a significant torque on the wheel, leading to premature failure. If the wheel is symmetrically actuated, the contact point with the ground does not move along the axle and the wheel does not experience any adverse torques.

4.2 Custom Robotics Controller Design

The proof-of-concept robot required the ability to drive four DC motors, four servos, and read four square waves generated by the encoders. A low-cost commercial robot controller that could provide the necessary functions did not exist, so a custom controller for the robot was designed around the Freescale K64F Freedom Board.

The K64F is a low-cost development board for the Freescale Kinetis K64 series Cortex-M4F ARM processor. The processor on the Freedom Board runs at 120 MHz, has an onboard FXOS8700CQ accelerometer, a microSD slot, an Ethernet port, and exposes 32 general purpose input-output (GPIO) pins. Of the 32 GPIO pins, twelve can be configured as 'Flex Timer Module' (FTM) channels. The FTM channels can detect rising and falling edges on input pins or output a Pulse Width Moduluated (PWM) signal. The PWM generation or input capture happen independently of the main processing loop; code time is not spent polling the inputs or generating a PWM signal. Four of the FTM channels were used to generate the PWM signals to drive

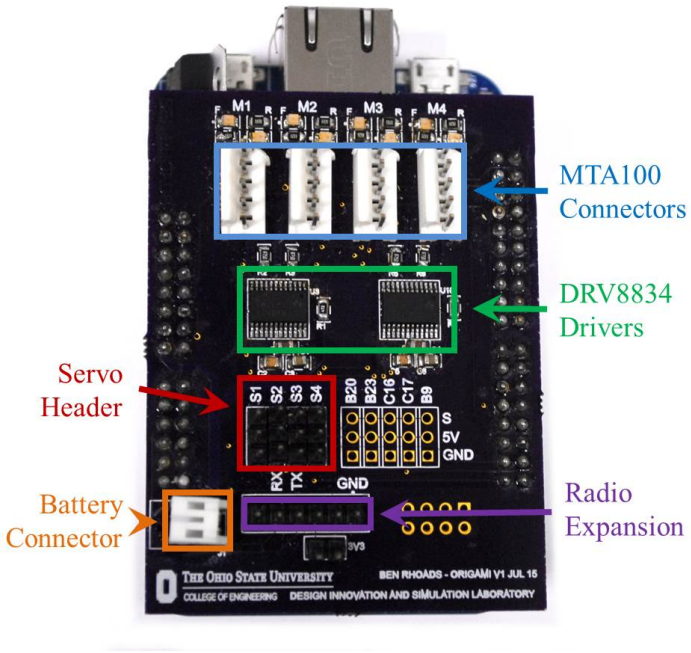

Figure 4.6: Custom Expansion Board

the servo actuators, four of the channels were used to generate the PWM signals to drive the DC motors, and the remaining four channels were used to capture the motor encoder output. The FXOS8700CQ accelerometer was used to detect the tilt and orientation of the robot.

The K64F alone is not capable of driving motors. Each GPIO pin is only capable of sourcing 25 mA of current and each of the Roomba motors drew approximately 200mA of current at startup. To allow the K64F to drive motors, a custom expansion board, shown in Figure 4.6 was designed and fabricated. The schematic and routing diagram of the board are available in Appendix E.

The custom expansion board features two Texas Instruments DRV8834 motor drivers. The DRV8834 was selected because each driver was capable of driving two

DC motors, the components were low cost, and the DRV8834 met the current requirements for the design. LEDs were attached in parallel to the motor outputs to show the direction the motor should be spinning for debugging purposes. TE Connectivity MTA 100 connectors were used to attach the Roomba motors to the board. Header pins were broken out for the four servo motors. The board also has a connector for a 2S Lithium Polymer battery to power the robot. Additionally, the board has a Universal Asynchronous Receiver/Transmitter (UART) port broken out to allow for future expansion with Bluetooth or Wi-Fi radios.

The robot was programmed using Freescale's Processor Expert inside of Kinetis Design Studio. Processor Expert allowed the proof-of-concept application to be developed quickly with reusable code components.

A simple HTML5 user interface was developed to control the robot. A small application written in Python served the HTML5 user interface, hosted a small websockets server, and communicated with the robot via UART. The user interface communicated via websockets with the Python application which then parsed the user requests and relayed the information to the robot.

4.3 Suspension, Transmission, and Steering

With four deformable wheels, the functions of suspension, transmission, and steering were accomplished without dedicated mechanisms.

By decreasing the wheel radius on one side of the robot and increasing the radius on the other side, the robot was able to steer. An example of the wheel diameters to turn to the right is shown in Figure 4.7. The wheel on the right of the vehicle had a smaller radii, thus a lower forward velocity, than the wheels on the left side. The

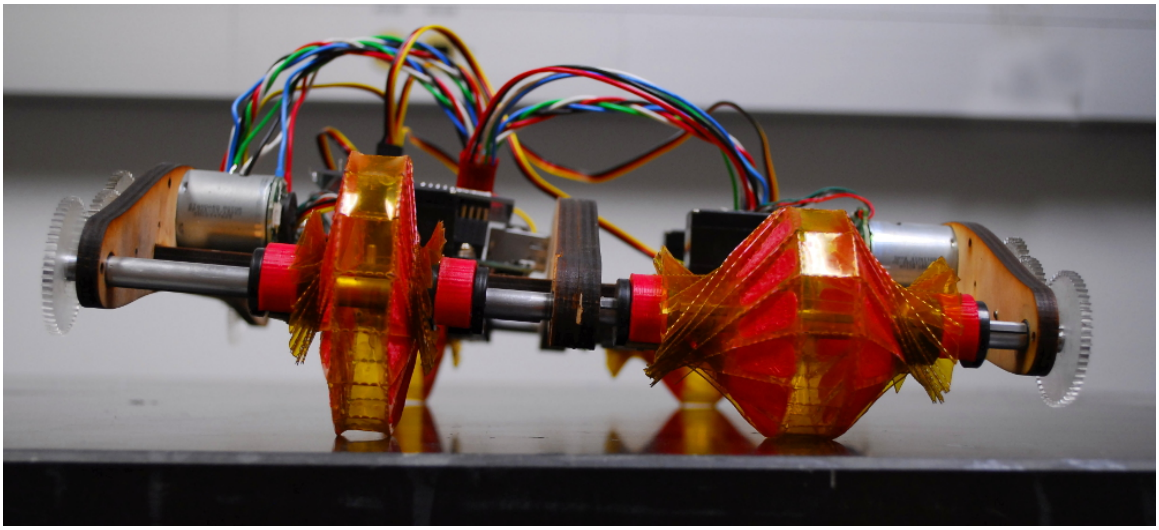

Figure 4.7: Wheel Configuration to Turn to the Right

velocity imbalance between the two sides of the vehicle caused the robot to turn with the turning radius R given by Equation 4.2 [30]. As the difference in the wheel radii becomes larger, the robot can make sharper turns.

$$R = K\frac{r_R + r_L}{\Delta r} \tag{4.2}$$

K	Proportionality Constant
r_R	Radius of Right Wheels
r_L	Radius of Left Wheels
Δr	Difference in Wheel Radii

Since the wheels were driven by PWM regulated electrical motors, the velocity imbalance could have been accomplished by changing the speeds of the respective wheels directly. However, to demonstrate that the deformation of the wheels could induce steering the motors were held at constant velocities. The combination of changing shaft speed and wheel radius was not explored but has potential to increase the turning radius of the vehicle. Combined, decreasing the wheel diameter and

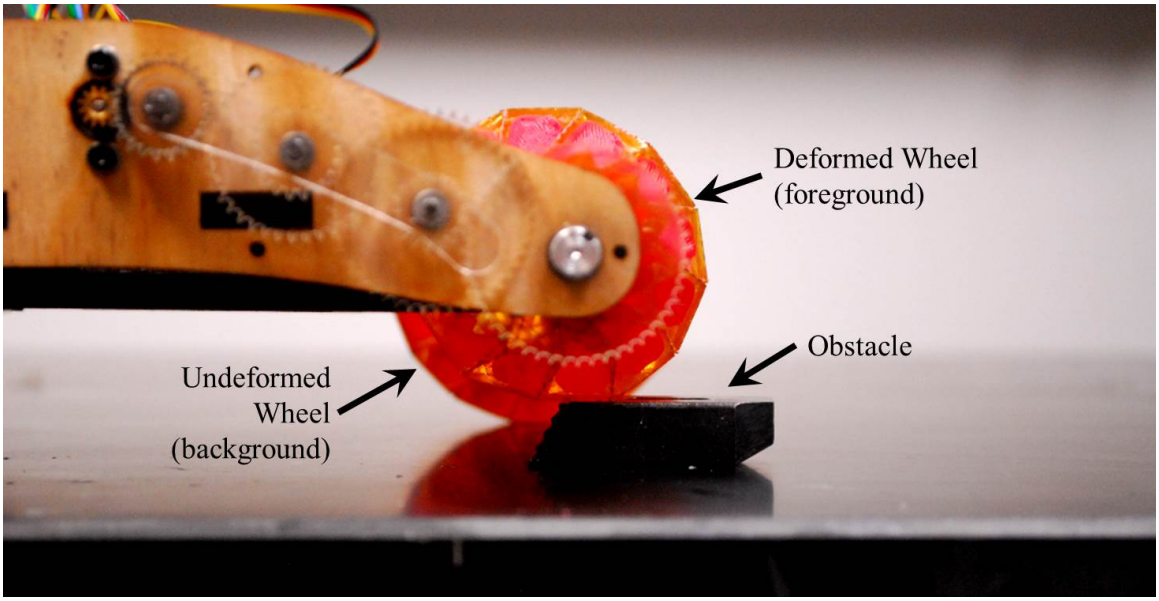

Figure 4.8: Wheel Deformation as An Obstacle is Encountered

decreasing the speed of the motor can produce a tighter turn than if the two systems are used independently.

The deformable wheels functioned as a suspension by increasing or decreasing in size to accommodate obstacles. In Figure 4.8 the wheel going over the obstacle decreased in size to keep the chassis level. Ideally, the robot uses data from the accelerometer to determine when an obstacle is encountered. For this proof-of-concept demonstration of the deformable wheel, the obstacle was placed a known distance ahead of the robot and the wheel deformed after the known distance was traveled.

Using the deformable wheels as a transmission was accomplished by increasing or decreasing the diameters of all four wheels simultaneously. Since forward velocity and rotational velocity are related by $v = r\omega$, as the wheel diameter increased, the forward velocity increased proportional to Δr. Similarly, decreasing the wheel

diameter proportionally decreased the forward velocity. The force required to stall the wheel also changed as the wheel diameter changed; at lower diameters more force was required to stall the wheel than at larger diameters since $\tau = rF$.

For all three functions, having larger radial deformations improves performance. When Δr is maximized, the robot is capable of steering into sharper turns. Similarly, the changes in forward velocity from using the wheels as a transmission are directly proportional to Δr. The maximum size of the obstacle that is able to be overcome by a deformable wheel suspension is given by Δr.

Chapter 5: Contributions and Future Work

An origami pattern was shown in Chapter 2 that can function as a deformable wheel. The design is self-intersecting and does not require a glued edge. The deformed radius of the wheel can theoretically be 50% of the undeformed radius. However, a closed form solution to describe the wheel efficiency was not found. Additionally, a full mathematical model of the deformation mechanism was not obtained and should be derived.

The novel 3D printed manufacturing method presented in Chapter 3 improves upon existing origami prototyping methods; however the process is limited to origami patterns that fit on a 3D printer print bed. With careful planning, it may be possible to print a portion of a design, move it on the print bed, and print the remaining portion. If printing portions of the origami pattern in this fashion can be made to work, the 3D printing method could scale to any sized origami pattern. Additionally, the polyester flexure used in the manufacturing method stores spring energy. For some origami mechanisms the spring energy is undesirable and increases the amount of force required to actuate the mechanism. Changing the amount of perforation or partially cutting through the polyester flexure along fold lines are two possible ways to reduce the energy storage and should be explored further.

The three functions of suspension, transmission, and steering were shown to be encapsulated by four deformable wheels in Chapter 4. However, a complete control system for the robot was not developed; the suspension, transmission, and steering were tested independently. A sophisticated control system could be written that would dynamically respond to obstacles, improve steering capability by increasing or decreasing shaft speed along with the wheel diameters, and compensate for the decreased linear velocity of a wheel deforming to absorb an obstacle by changing the shaft speed.

While the deformable wheel presented in this thesis was used to demonstrate a working transmission, suspension, and steering mechanism for a small robot, the wheel is not limited to those tasks. For example, two deformable wheels connected by a belt form a Continuously Variable Transmission. Additionally, situations where torque and speed requirement change drastically, such as a vehicle in a drag race, would benefit from a deformable wheel. By creating a deformable wheel using origami and developing a rapid prototyping process for origami mechanisms, exploring the potential applications of deformable wheels has been made easier.

There is no real ending. It's just
the place where you stop the story.

Frank Herbert

Appendix A: Origami Fold Patterns

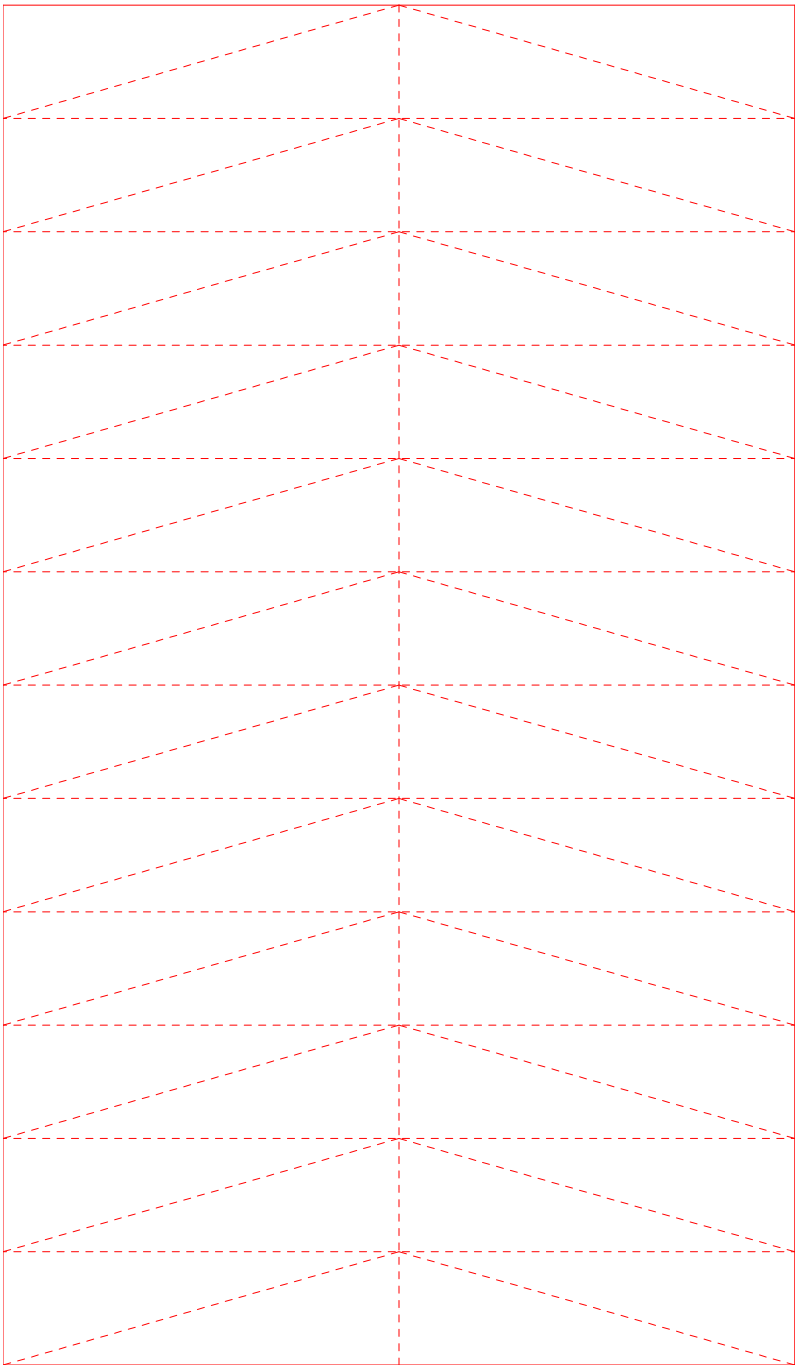

Figure A.1: Original Jeff Benyon Fold Pattern

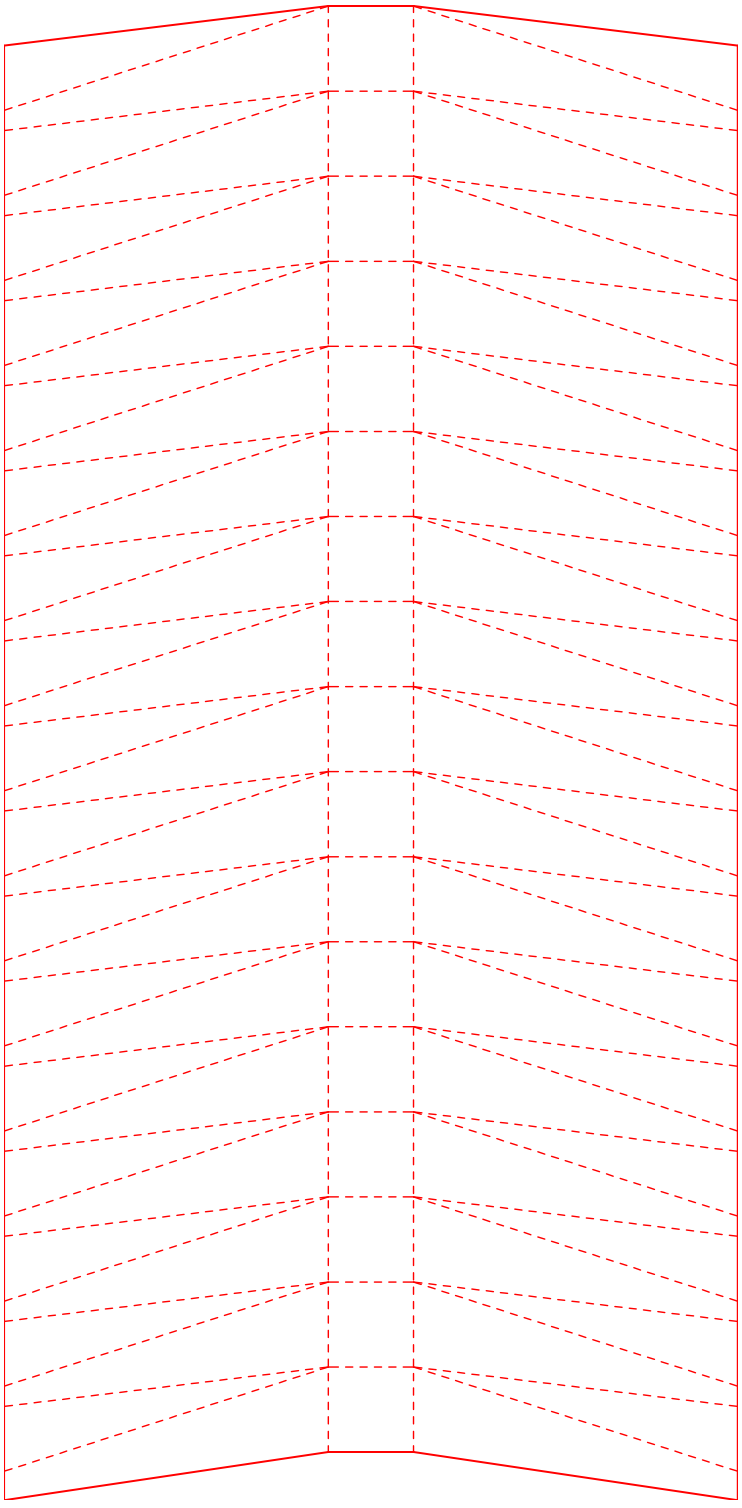

Figure A.2: Full Deformable Wheel Pattern

Appendix B: Detailed Calculations And Derivations

B.1 Geometric Derivations

B.1.1 n-Sided Polygon

An n-sided regular polygon can be treated as an axisymmetric rotation of isosceles triangles, shown below. For reasons made obvious in Section B.1.2, the n-sided polygon was parameterized by h, the edge length, l, the effective 'radius', and 2α, the interior angle of the isosceles triangles.

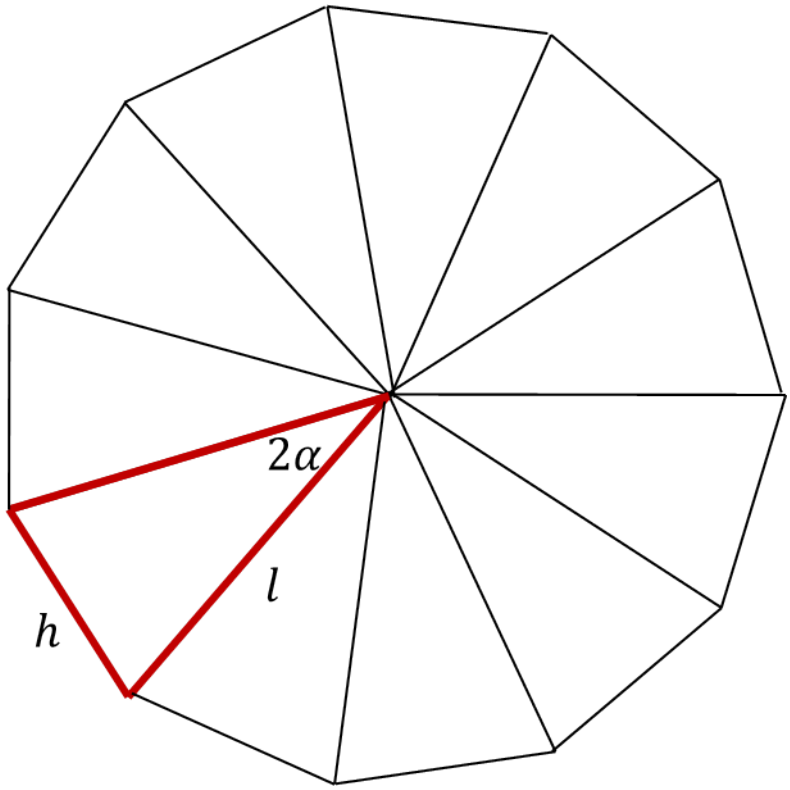

Since the n-sided polygon is regular, the interior angles represented by 2α must add up to 2π.

$$n = \frac{2\pi}{2\alpha} \tag{B.1}$$

Since the triangles are isosceles, the angle *alpha* is given by

$$\alpha = \sin^{-1}\left(\frac{h}{2l}\right) \tag{B.2}$$

Combining Equations B.1 and B.2,

$$n = \frac{\pi}{\sin^{-1}\left(\frac{h}{2l}\right)} \tag{B.3}$$

As the wheel deforms, the number of sides of the polygon changes. The coordinate frame below was established to link the axial deformation, x to the change in n and the effective radius l.

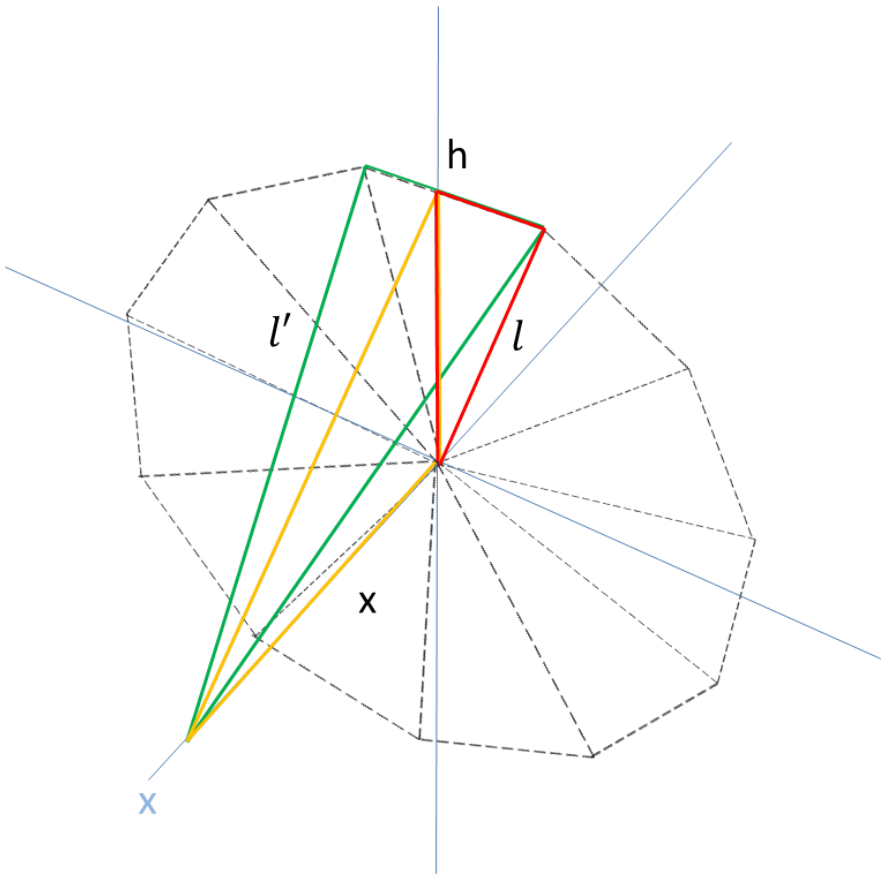

Recognizing that l', l, and x form a right triangle:

$$l'^2 = l^2 + x^2$$

$$l = \sqrt{l'^2 - x^2} \tag{B.4}$$

When $x = 0$, $l' = l$, thus l' is the initial effective radius of the n-sided regular polygon.

Introducing Equation B.4 into Equation B.3:

$$n = \frac{\pi}{\sin^{-1}\left(\frac{h}{2\sqrt{l'^2 - x^2}}\right)} \tag{B.5}$$

B.1.2 Modified Wheel

Beginning with two of the modified fold pattern units, α and β are assigned to interior angles. Five points $(A - E)$ are also labeled to help communicate which lines are being folded. The usual design parameters, h, w, and δ are also labeled.

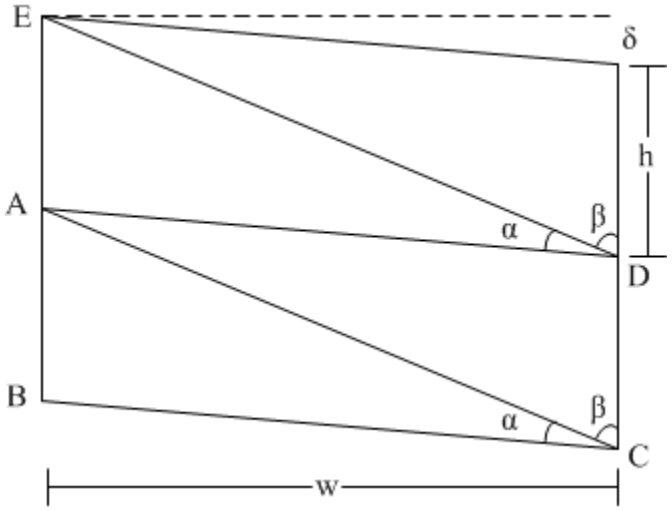

From this description of the fold pattern, it is possible to relate α and β in terms of the design parameters h, w, and δ.

$$\alpha = \tan^{-1}\left(\frac{h+\delta}{w}\right) - \tan^{-1}\left(\frac{\delta}{w}\right) \tag{B.6}$$

$$\beta = \frac{\pi}{2} - \tan^{-1}\left(\frac{h+\delta}{w}\right) \tag{B.7}$$

Folding the pattern over line AC:

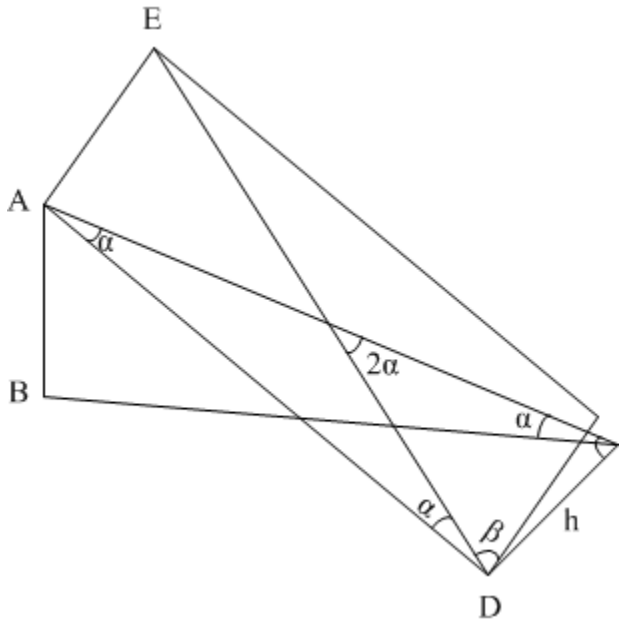

Minor geometric features have been labeled, namely the interior angle 2α.

Imagining a third unit, line ED is folded over:

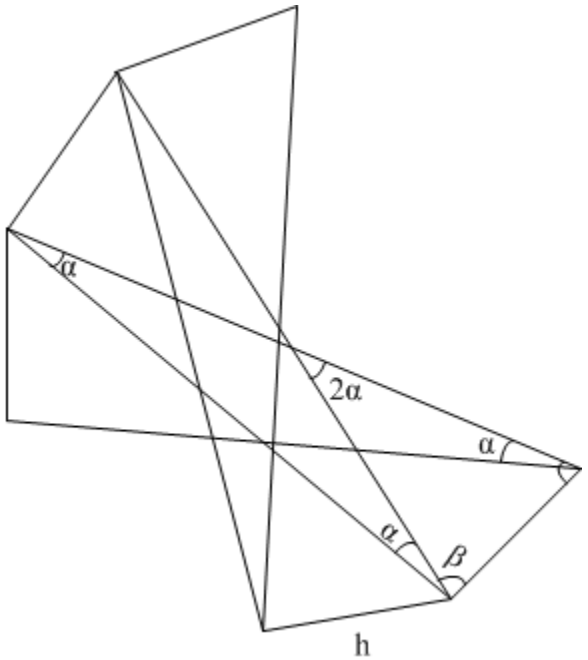

It is important to notice the geometry formed from folding over line AC and line ED are identical, but rotated. Both folds formed similar triangles, highlighted below in bold. If the pattern had continued to be folded, the triangles below would have continued to be made and form the n-sided polygon that is the wheel.

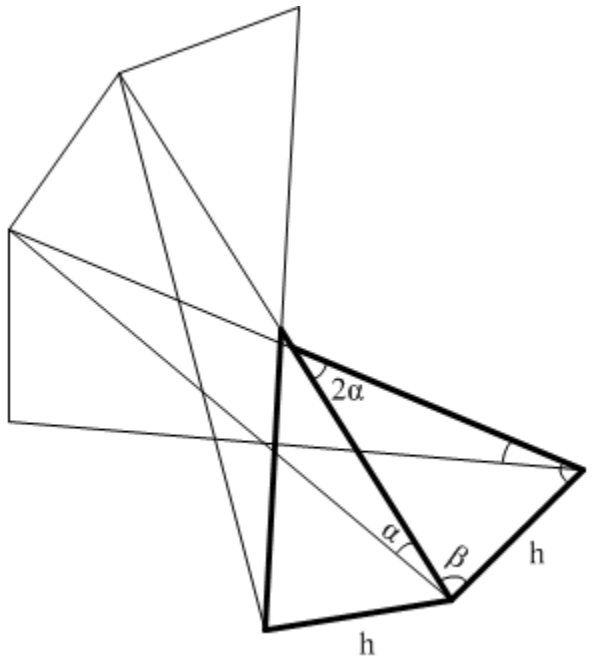

Introducing l_1 and l_2, the side lengths of the triangles created from folding, and γ, the third interior angle:

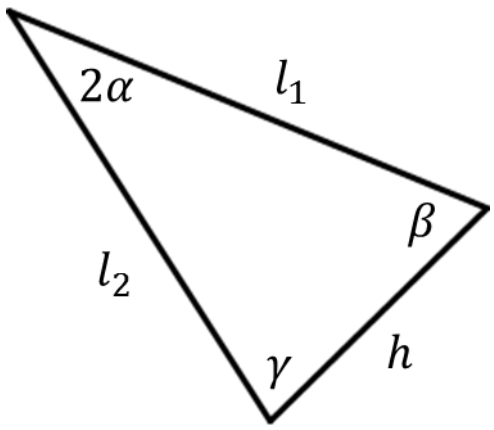

Since h, 2α, and β, are known, the law of sines was used to determine l_2 and l_1:

$$\frac{h}{\sin 2\alpha} = \frac{l_2}{\sin \beta}$$

From the first geometric definition,

$$\sin \beta = \frac{w}{\sqrt{(\delta + h)^2 + w^2}}$$

Thus,

$$\frac{h}{\sin 2\alpha} = \frac{l_2 \sqrt{(\delta + h)^2 + w^2}}{w}$$

Solving for l_2:

$$l_2 = \frac{wh}{\sqrt{(\delta + h)^2 + w^2}} \csc 2\alpha \tag{B.8}$$

l_1 is solved in a similar manner with the law of sines. From the definition of a triangle, $\gamma = \pi - 2\alpha - \beta$.

$$l_1 = \frac{\sin\gamma}{\sin(2\alpha)}h \tag{B.9}$$

The triangles produced by the modified fold pattern do not form isosceles triangles like the original fold pattern; the triangles are skewed to one side. In order to relate the modified pattern with the equations derived for an n-sided regular polygon in Section B.1.1, it is desired to find the equivalent isosceles triangle, shown as a dashed line below. h' is the height of both triangles and L is the edge length of the representative isosceles triangle. The end points of the two triangles are separated by $\delta/2$.

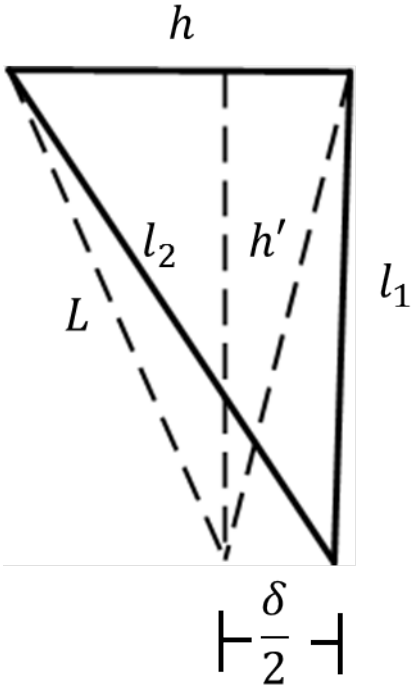

The triangles are related by their heights, h'. The area formula was used to find the h' of the modified triangle. The formula for area when the base and height are known is:

$$A = \frac{1}{2}bh$$

While Heron's Formula gives the area of a triangle when all edge lenghts are known, which is the case of the modified triangle.

$$A = \sqrt{s\left(s-a\right)\left(s-b\right)\left(s-c\right)}$$

$$s = \frac{1}{2}\left(a+b+c\right)$$

$$A = \frac{1}{4}\sqrt{4a^2b^2 - \left(a^2+b^2-c^2\right)^2}$$

Equating Heron's Formula and the simpler area formula allows the three known edge lengths to be used to find the height of the triangle, h'.

$$A = \frac{1}{4}\sqrt{4h^2l_2^2 - \left(h^2+l_2^2-l_1^2\right)^2} = \frac{1}{2}hh' \tag{B.10}$$

Solving Equation B.10 for h' results in:

$$h' = \frac{\sqrt{4h^2l_2^2 - \left(h^2+l_2^2-l_1^2\right)^2}}{2h}$$

Which can be used to find L:

$$L = \sqrt{h^2+h'^2} = \sqrt{h^2 + \left(\frac{\sqrt{4h^2l_2^2 - \left(h^2+l_2^2-l_1^2\right)^2}}{2h}\right)^2} = r \tag{B.11}$$

Since L is known, the Equations derived in Section B.1.1 can be used in terms of the modified fold pattern. Using the value of r for the modified spring pattern in Equation B.1, the number of sides n becomes:

$$n = \frac{\pi}{\sin^{-1}\left(\frac{h}{2r}\right)} = \frac{\pi}{\sin^{-1}\left(\frac{h}{2\sqrt{h^2 + \left(\frac{\sqrt{4h^2l_2^2 - \left(h^2 + l_2^2 - l_1^2\right)^2}}{2h}\right)^2}}\right)} \tag{B.12}$$

Substituting Equations B.6, B.7, B.8, and B.9 into Equation B.12 results in the following heavily simplified equation:

$$n = \frac{\pi}{\sin^{-1}\left(\frac{h}{\sqrt{-\frac{h^2w^2\left(\delta h + w^2\right)}{\left(\delta(\delta+h)+w^2\right)^2} + h^2 + \frac{hw^2(2\delta+h)}{\delta(\delta+h)+w^2} + w^2 - 4x^2}}\right)} \tag{B.13}$$

Equation B.13 has several domain limiting factors, namely the $\sin^{-1}$, the denominator inside of the $\sin^{-1}$, and the denominator under π. To simplify analysis, δ was assumed to be 0.

Inspecting sin^{-1}, which has a domain from $-1 < z < 1$:

$$-1 < \frac{h}{\sqrt{h^2 + w^2 - 4x^2}} < 1$$

$$-\sqrt{h^2 + w^2 - 4x^2} < h < \sqrt{h^2 + w^2 - 4x^2}$$

$$h^2 < h^2 + w^2 - 4x^2$$

$$x^2 < \frac{w^2}{4}$$

$$x < \frac{w}{2}$$

$w/2$ is the radius of the wheel - x cannot physically be larger than the radius of the wheel without the wheel breaking. When $x = w/2$, the radius of the wheel is 0.

Looking at the denominator under π, the $\sin^{-1}$ term cannot equal 0. This occurs when $h = 0$, which is physically trivial since if $h = 0$, the wheel does not exist.

B.1.3 Wheel Optimization

The 'critical fold' was approximated by the following diagram:

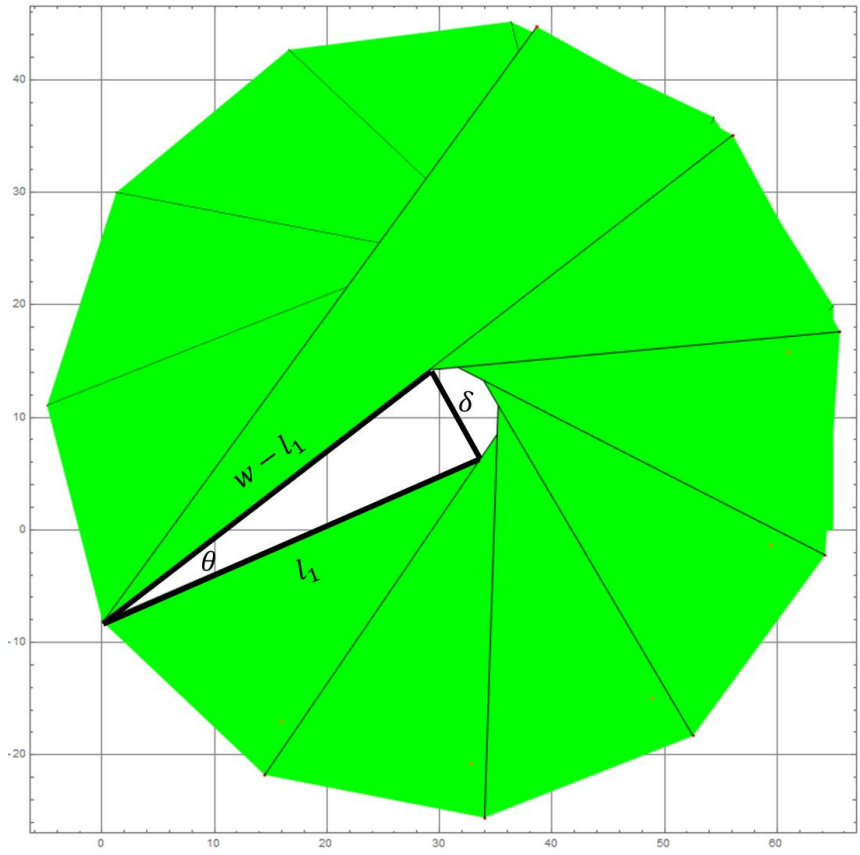

Using the law of cosines, θ was found to be

$$\theta = \cos^{-1}\left(\frac{(w - l_1)^2 + l_1^2 - \delta^2}{2\,(w - l_1)\,l_1}\right) \tag{B.14}$$

The number of sides that have been folded at the critical point is

$$n' = \frac{\pi + \theta}{2\alpha} \tag{B.15}$$

From the n-sided regular polygon approximation, the effective radius of a polygon is given by:

$$r = \frac{h}{2\sin^{-1}\left(\frac{\pi}{n}\right)} \tag{B.16}$$

The percentage of radius change from the undeformed to fully deformed wheel can then be expressed as η, shown in Equation B.17.

$$\eta = \frac{\sin\left(\frac{\pi}{n}\right)}{\sin\left(\frac{\pi}{n'}\right)} \tag{B.17}$$

The number of sides required to form a complete wheel is given by Equation B.18 where α, given by B.6 is a function of the design parameters. The interior angles of the triangles forming an n-sided polygon sum to 2π, and the interior angle of triangle is 2α.

$$n = \frac{2\pi}{2\alpha} \tag{B.18}$$

Substituting Equation B.15 and Equation B.18 into Equation B.17:

$$\eta = \frac{\sin(\alpha)}{\sin\left(\frac{2\pi}{\pi+\theta+1}\right)} \tag{B.19}$$

B.2 Laminate Moment of Inertia

The 3D printed wheel was modeled as a 3-ply anisotropic laminate.

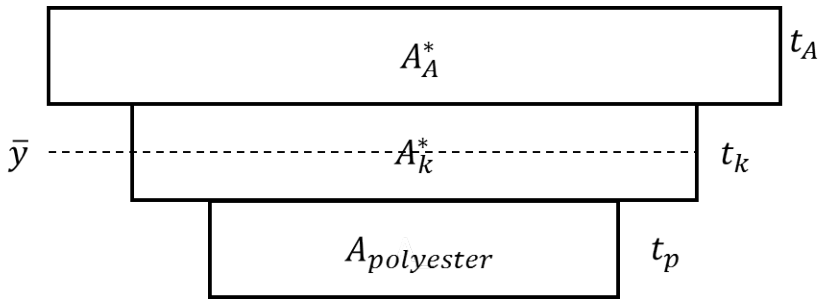

$$A^* = \frac{E_{poly}}{E} tw \tag{B.20}$$

A^*	Effective Area
E	Young's Modulus of Non Polyester Material
t	Layer Thickness
w	Layer Width

The equivalent areas for the polyimde and ABS layers were calculated relative to the polyester base. A nominal width of 1 was selected since the calculated moment of inertias were being relatively compared.

$$A_A^* = \frac{E_{poly}}{E_A} t_A w = \frac{3.5\text{GPa}}{1.8\text{GPa}} \left(4.57 \times 10^{-4}\text{m}\right) (1\text{m}) = 8.88 \times 10^{-4}\text{m}^2 \tag{B.21}$$

A_A^*	Effective Area of ABS
E_A	Young's Modulus of ABS [27]
t_A	ABS Layer Thickness

$$A_K^* = \frac{E_{poly}}{E_k} t_k w = \frac{3.5\text{GPa}}{2.5\text{GPa}} \left(4 \times 10^{-5}\text{m}\right) (1\text{m}) = 5.6 \times 10^{-5}\text{m}^2 \tag{B.22}$$

A_K^* Effective Area of Polyimide
E_K Young's Modulus of Polyimide [7]
t_K Polyimide Layer Thickness

The area moment of inertia of the laminate is the sum of the moment of intertias of its parts.

$$I = I_A + I_K + I_P \tag{B.23}$$

I Effective Moment of Inertia
I_A Moment of Inertia of ABS
I_K Moment of Inertia of Polyimide
I_P Moment of Inertia of Polyester

Moment of Inertia of the ABS section:

$$I_A = \frac{1}{12}\frac{A_A^*}{t_A}t_A^3 + A_A^* d_{\bar{y}}$$

$d_{\bar{y}}$ Distance from $\bar{y}$

$$I_A = \frac{1}{12}\frac{8.88\times10^{-4}\mathrm{m}^2}{4.57\times10^{-4}\mathrm{m}}\left(4.57\times10^{-4}\mathrm{m}\right)^3 + 8.88\times10^{-4}\mathrm{m}^2\frac{1}{2}\left(4.57\times10^{-4}\mathrm{m} + 4\times10^{-5}\mathrm{m}\right) = 3.395\times10^{-8}\mathrm{m}^4$$

Moment of Inertia of the Polyimide section:

$$I_K = \frac{1}{12}\frac{A_K^*}{t_K}t_K^3$$

$$I_K = \frac{1}{12}\frac{5.6\times10^{-5}\mathrm{m}^2}{4\times10^{-5}\mathrm{m}}\left(4\times10^{-5}\mathrm{m}\right)^3 = 7.46\times10^{-15}\mathrm{m}^4$$

Moment of Inertia of the Polyester section:

$$I_P = \frac{1}{12}t_P^3 + A_P d_{\bar{y}}$$

$$I_P = \frac{1}{12}\left(8.89\times10^{-5}\mathrm{m}\right)^3 + \left(8.89\times10^{-5}\mathrm{m}\right)\frac{1}{2}\left(8.89\times10^{-5}\mathrm{m} + 4\times10^{-5}\mathrm{m}\right) = 5.729\times10^{-9}\mathrm{m}^4$$

Moment of Inertia of Laminate:

$$I = I_A + I_K + I_P = 3.395 \times 10^{-8}\text{m}^4 + 7.46 \times 10^{-15}\text{m}^4 + 5.729 \times 10^{-9}\text{m}^4 = 5.854 \times 10^{-9}\text{m}^4$$

Finding the Moment of Inertia of a wheel made from polyester:

$$I_{poly} = \frac{1}{12}bh^3 = \frac{1}{12}\left(1\text{m}\right)\left(8.89 \times 10^{-5}\text{m}\right)^3 = 5.85 \times 10^{-14}\text{m}^4$$

Comparing:

$$\eta = \frac{I}{I_{poly}} = \frac{5.854 \times 10^{-9}\text{m}^4}{5.85 \times 10^{-14}\text{m}^4} = 99998 \approx 10^5$$

B.3 Wheel Stresses

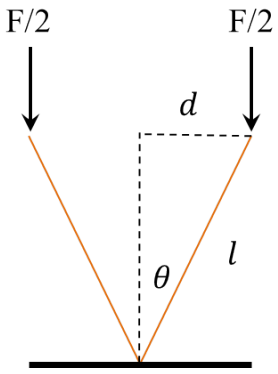

Figure B.1: Free Body Diagram of Wheel

$$\sigma = \frac{F}{A^*} + \frac{Mc}{I} \tag{B.24}$$

Calculating the effective area and moment of inertia for the polyester/polyimide portion of the wheel.

$$A^* = \frac{3.5\text{GPa}}{2.5\text{GPa}} \left(4 \times 10^{-5}\text{m}\right) (0.015\text{m}) = 8.4 \times 10^{-7}\text{m}^2$$

$$I = \frac{1}{3} (0.015\text{m}) \left[\left(8.89 \times 10^{-5}\text{m}\right)^3 + \left(4 \times 10^{-5}\text{m}\right)^3 \right] = 3.83 \times 10^{-15}\text{m}^4$$

The angle between the applied force and the axis of the wheel material is given by

$$\theta = \sin^- 1 \left(\frac{d}{l}\right) = \sin^- 1 \left(\frac{0.0127\text{m}}{0.040\text{m}}\right) = 18.51\text{deg}$$

Calculating the stress in the wheel:

$$\sigma = \frac{F}{A^*} + \frac{Mc}{I} = \frac{F\cos\theta}{A^*} + \frac{F\sin(\theta)\,lc}{I} \tag{B.25}$$

Using the average yield load for the 3D printed wheel of 11.97N and distributing it over 4 wheels, $F = 2.99\text{N}$. Since the applied load is distributed by the axle to the two portions of the wheel making contact with the ground, $F = F/2 = 1.49\text{N}$.

$$\sigma = \frac{1.49\text{N}\cos(18.51\text{deg})}{8.4\times10^{-7}\text{m}^2} + \frac{1.49\text{N}\sin(18.51\text{deg})\,(0.04\text{m})\left(\frac{1}{2}4\times10^{-5}\text{m}\right)}{3.83\times10^{-15}\text{m}^4} = 100.5\text{MPa}$$

B.4 Composite Yield Stress

From [23], the yield stress of a composite can be approximated using the rule of mixtures:

$$\sigma_y = \nu_1\sigma_{y1} + \nu_2\sigma_{y2} \tag{B.26}$$

σ_y	Distance from $\bar{y}$
ν_1	Volume Fraction of Material 1
σ_{y1}	Yield Strength of Material 1
ν_2	Volume Fraction of Material 2
σ_{y2}	Yield Strength of Material 2

For the polyester/polyimide sheet the material properties are [8, 7]:

$$\sigma_{y_{polyester}} \approx 83\text{MPa}$$

$$\sigma_{y_{polyimide}} \approx 138\text{MPa}$$

Since the polyester and polyimide are equal widths, the volume fraction of the sheet is a ratio of the thicknesses.

$$\nu_{polyester} = \frac{t_{polyester}}{t_{polyester} + t_{polyimide}} = \frac{8.89 \times 10^{-5}\text{m}}{8.89 \times 10^{-5}\text{m} + 4 \times 10^{-5}} = 0.689$$

$$\nu_{polyimide} = \frac{t_{polyimide}}{t_{polyester} + t_{polyimide}} = \frac{4 \times 10^{-5}\text{m}}{8.89 \times 10^{-5}\text{m} + 4 \times 10^{-5}} = 0.31$$

$$\sigma_y = 0.689\,(83\text{MPa}) + 0.31\,(138\text{MPa}) = 100.05\text{MPa}$$

Appendix C: Visualization of Shape Deposition Manufacturing Process

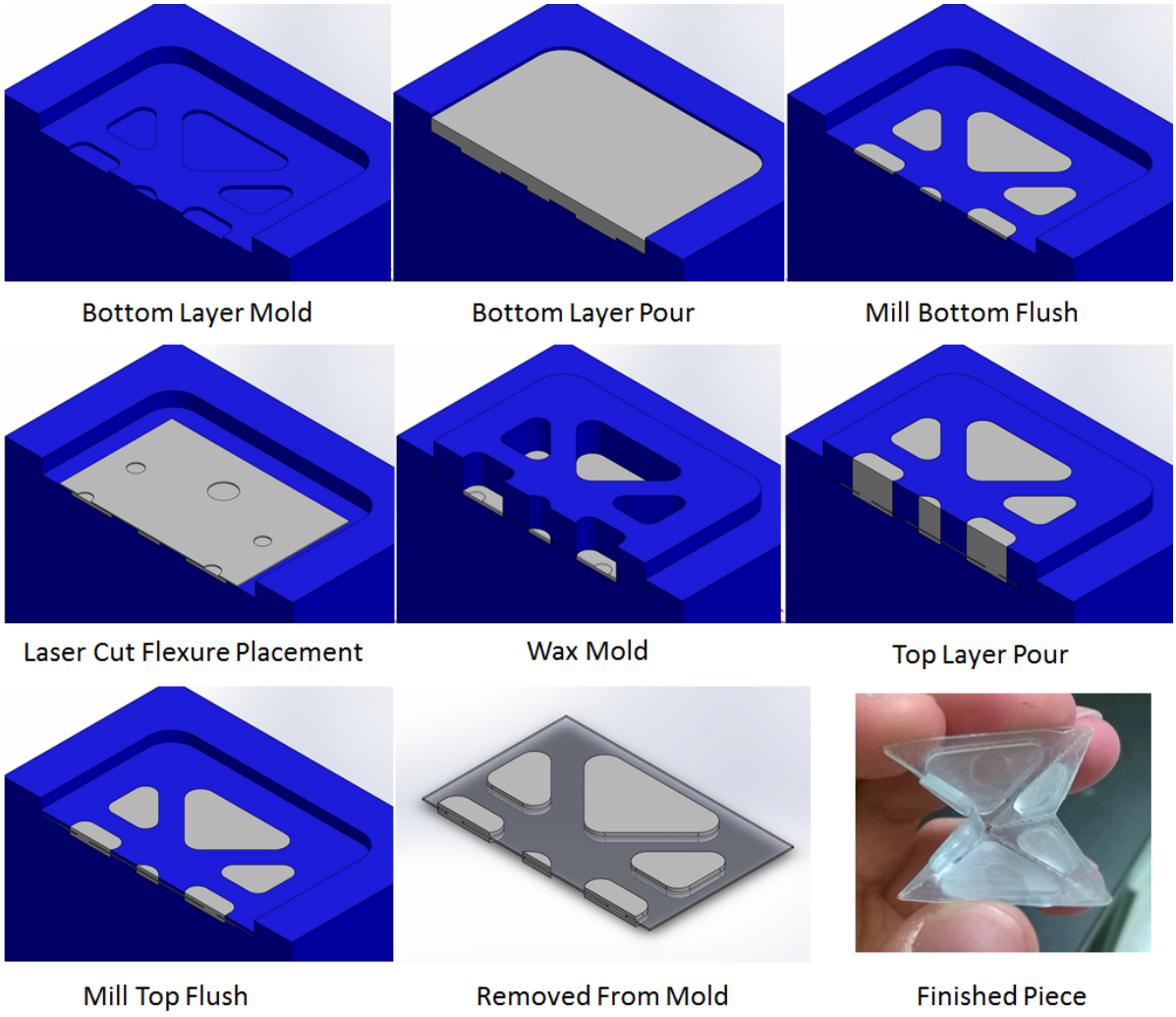

Figure C.1: Visualization of Shape Deposition Manufacturing Process

Appendix D: Load Testing Data

Table D.1: Paper Wheel Yielding and Failure Loads

	Yield Loads (N)				Failure Load (N)
Test Case	Front Right	Front Left	Back Right	Back Left	
1	11.985	12.034	12.034	12.083	37.191
2	11.985	11.985	11.985	11.936	38.132
3	12.083	11.985	12.034	12.083	37.505
4	12.034	12.034	12.034	12.034	37.897
5	11.936	12.034	12.034	12.034	37.691

Table D.2: Polyester Wheel Yielding and Failure Loads

	Yield Loads (N)				Failure Load (N)
Test Case	Front Right	Front Left	Back Right	Back Left	
1	28.459	29.606	29.165	29.606	29.606
2	32.389	20.992	32.389	32.389	32.389
3	31.154	24.284	31.154	27.528	31.154
4	30.968	30.968	25.186	30.968	30.968
5	30.478	24.618	30.478	30.478	30.478

Table D.3: 3D Printed Wheel Yielding and Failure Loads

	Yield Loads (N)				Failure Load (N)
Test Case	Front Right	Front Left	Back Right	Back Left	
1	75.293	75.293	75.293	75.293	75.293
2	78.616	78.616	78.616	78.616	78.616
3	76.812	76.812	76.812	76.812	76.812

Appendix E: Robot Controller Schematic

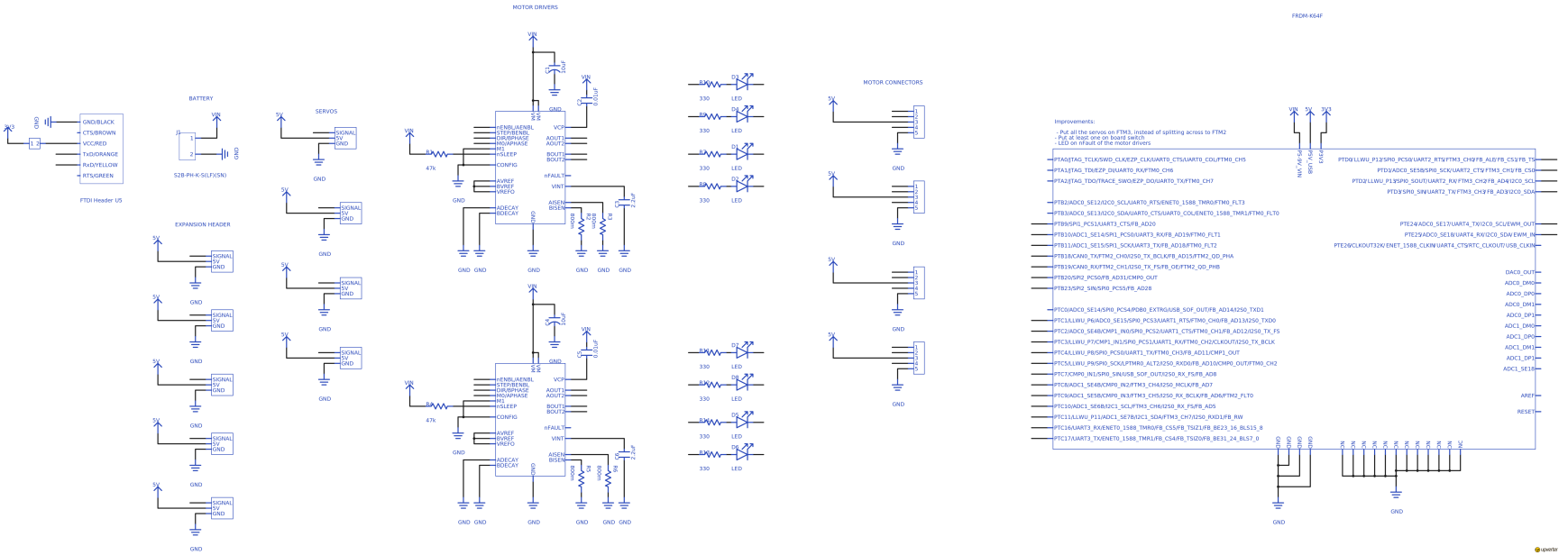
FTDI Header U5
GND/BLACK
CTS/BROWN
VCC/RED
TxD/ORANGE
RxD/YELLOW
RTS/GREEN
BATTERY
S2B-PH-K-S(LF)(SN)
EXPANSION HEADER
SERVOS
MOTOR DRIVERS
MOTOR CONNECTORS
FRDM-K64F
Improvements:
- Put all the servos on FTM3, instead of splitting across to FTM2
- Put at least one on board switch
- LED on nFault of the motor drivers
upverter

Bibliography

[1] Sunil K. Agrawal. "A Three-Wheel Vehicle with Expanding Wheels: Differential Flatness, Trajectory Planning, and Control". In: *Proceedings of the 2001 IEEE International Conference on Intelligent Robots and Systems*. IEEE. 2003.

[2] Sunil K. Agrawal. "Polyhedral Single Degree-of-Freedom Expanding Structures". In: *Proceedings of the 2001 IEEE International Conference on Robotics and Automation*. IEEE. 2001.

[3] Lifeng Zhou et al. "DNA Origami Compliant Nanostructures with Tunable Mechanical Properties". In: *ACS Nano* 8 (2014).

[4] Daniel M Aukes et al. "An Analytic Framework for Developing Inherently Manufacturable Popup Laminate Devices". In: *Smart Materials and Structures* 23 (2014).

[5] Jorge G Cham, Beth L. Pruitt, and et al Mark R. Cutkosky. "Layered Manufacturing With Embedded Components: Process Planning Considerations". In: *Proceedings of 1999 ASME Design Engineering Technical Conference*. ASME. 1999.

[6] *Creating ABS Glue*. URL: `http://wiki.solidoodle.com/creating-abs-glue` (visited on 02/17/2015).

[7] DuPont Films. *Kapton Polyimide General Specifications*. 2003.

[8] DuPont Films. *Mylar Polyester Film Product Information*. 2003.

[9] Russell C Hibbeler. *Mechanics of Materials*. 8th. Prentice Hall, 2010.

[10] Hoover. "Fast scale prototyping for folded millirobots". In: *Proceedings of the IEEE 2008 International Conference on Robotics and Automation*. IEEE. May 2008.

[11] Alan R. Jones. "An Experimental Investigation of the In-Plane Elastic Moduli of Paper". PhD thesis. The University of Colorado, 1967.

[12] et al Kevin C. Francis. "From Crease Pattern to Product: Considerations to Engineering Origami-Adpated Designs". In: *Proceedings of the ASME 2014 International Design Engineering Technical Conferences & Computers and Information in Engineering Conference*. ASME. 2014.

[13] Biomimetic Millisystems Lab. *Prototyping Folding Robots*. URL: http://robotics.eecs.berkeley.edu/~ronf/Prototype/index.html (visited on 10/15/2015).

[14] Dae-Young Lee et al. "Fabrication of Origami Wheel using Pattern Embedded Fabric and its Application to a Deformable Mobile Robot". In: *2014 IEEE Internation Conference on Robotics & Automation*. IEEE. May 2014.

[15] Dae-Young Lee et al. "The Deformable Wheel Robot Using Magic-Ball Origami Structure". In: *Proceedings of the ASME 2013 International Design Engineering Technical Conferences & Computers and Information in Engineering Conference*. ASME. Aug. 2013.

[16] *Lewis Galoob Toys, Inc 'The Animal' Commerical*. URL: https://www.youtube.com/embed/-IRCaE3ks6Y (visited on 10/15/2015).

[17] *Makerbot Homepage*. URL: http://www.makerbot.com/ (visited on 11/09/2015).

[18] Michelin. *Michelin Tweel*. URL: http://michelintweel.com/ (visited on 10/15/2015).

[19] Seval Pinarbasi. "Buckling Analysis of Nonuniform Columns with Elastic End Restraints". In: *Journal of Mechanics of Materials and Structures* 7.5 (2012).

[20] Pavel L. Potapov and Edson P. da Silva. "Time Response of Shape Memory Alloy Actuators". In: *Journal of Intelligent Material Systems and Structures* 11 (2000).

[21] *ProfTweak - a Makerware profile editor*. URL: https://github.com/nothinglabs/proftweak (visited on 01/23/2015).

[22] *RepRap Wiki*. URL: http://www.reprap.org/wiki/RepRap (visited on 11/09/2015).

[23] David Roylance. *Mechanical Properties of Materials*. 2008.

[24] Cynthia Sung and Daniela Rus. *Foldable Joints for Foldable Robots*. Tech. rep. Massachusetts Institute of Technology.

[25] *The ReInvented Wheel*. URL: http://www.unusuallocomotion.com/pages/locomotion/the-wheel-reinvented.html (visited on 10/15/2015).

[26] *The Shape Deposition Manufacturing Process*. URL: http://www.cs.cmu.edu/~sdm/methodolgy.htm (visited on 10/16/2015).

[27] B.M. Tymrak, M. Kreiger, and J.M. Pearce. "Mechanical Properties of Components Fabricated with Open-Source 3-D printers Under Realistic Environmental Conditions". In: *Materials and Design* 58 (2014).

[28] *Using Polymers in SDM*. URL: http://bdml.stanford.edu/twiki/bin/view/Manufacturing/SDMUsingPolymers.html (visited on 11/08/2015).

[29] et al Wood R. J. "Microrobot Design Using Fiber Reinforced Composites". In: *Journal of Mechanical Design* 130 (2008).

[30] Xiaodong Wu, Min Xu, and Lei Wang. "Differential Speed Steering Control for Four-Wheel Independent Driving Vehicle". In: *Journal of Materials, Mechanics and Manufacturing* 1 (2013).

[31] Carter Hurd Yu She and Hai-Jun Su. "A Transformable Wheel Robot with A Passive Leg". In: *2015 IEEE International Conference on Intelligent Robots and Systems Proceedings*. IEEE. Sept. 2015.